

A Novel Hybrid Algorithm for Optimized Solutions in Ocean Renewable Energy Industry: Enhancing Power Take-Off Parameters and Site Selection Procedure of Wave Energy Converters

Hossein Mehdipour^a, Erfan Amini^b, Seyed Taghi (Omid) Naeeni^a, Mehdi Neshat^{c,d}

^a*School of Civil Engineering, College of Engineering, University of Tehran, Tehran 14179, Iran
hossein.mehdipour@ut.ac.ir; stnaeeni@ut.ac.ir*

^b*Department of Civil, Environmental and Ocean Engineering, Stevens Institute of Technology, Hoboken, New Jersey 07030, United States
eamini@stevens.edu*

^c*Center for Artificial Intelligence Research and Optimization, Torrens University Australia, Brisbane, QLD 4006, Australia
mehdi.neshat@torrens.edu.au*

^d*Faculty of Engineering and Information Technology, University of Technology Sydney, Ultimo, Sydney, 2007, NSW, Australia
mehdi.neshat@uts.edu.au*

Abstract

Ocean renewable energy, particularly wave energy, has emerged as a pivotal component for diversifying the global energy portfolio, reducing dependence on fossil fuels, and mitigating climate change impacts. This study delves into the optimization of power take-off (PTO) parameters and the site selection process for an offshore oscillating surge wave energy converter (OSWEC). The intricate interplay between waves and the energy conversion device results in nonlinear and transient responses in wave energy converters (WECs). Hence, there's a pressing need to optimize PTO parameters, ensuring that the device maximizes power absorption while evading potential damage or instability. However, the intrinsic dynamics of these interactions, coupled with the multi-modal nature of the optimization landscape, make this a daunting challenge. Addressing this, we introduce the novel Hill Climb - Explorative Gray Wolf Optimizer (HC-EGWO). This new methodology blends a local search method with a global optimizer, incorporating dynamic control over exploration and exploitation rates. This balance paves the way for an enhanced exploration of the solution space, ensuring the identification of superior-quality solutions. Further anchoring our approach, a feasibility landscape analysis based on linear water wave theory assumptions and the flap's maximum angular motion is conducted. This ensures the optimized OSWEC consistently operates within safety and efficiency parameters. Our findings hold significant promise for the development of more streamlined OSWEC power take-off systems. They provide insights for selecting the prime offshore site, optimizing power output, and bolstering the overall adoption of ocean renewable energy sources. Impressively, by employing the HC-EGWO method, we achieved an upswing of up to 3.31% in power output compared to other methods. This substantial increment underscores the efficacy of our proposed optimization approach. Conclusively, the outcomes offer invaluable knowledge for deploying OSWECs in the South Caspian Sea, where unique environmental conditions intersect with considerable energy potential.

Keywords: Ocean renewable energy, oscillating surge wave energy converter, power take-off optimization, Site selection, Meta-heuristic, Swarm intelligence algorithms

1. Introduction

The importance of ocean renewable energy cannot be overstated, as it offers a promising means to diversify the global energy portfolio, reduce dependence on fossil fuels, and mitigate the impacts of climate change [1]. Due to the vastness and untapped potential of the world's oceans, harnessing their power for sustainable electricity generation is critical for meeting the rising energy demands of an ever-growing global population. Furthermore, ocean energy

resources such as tidal, wave, and ocean thermal energy conversion (OTEC) exhibit lower variability and higher predictability compared to other renewable sources like wind and solar [2]. However, it is the ocean wave energy sector that has witnessed the most substantial advancements in recent years, with numerous ocean wave energy converters (WECs) under development and testing [3, 4]. These devices capture and transform the kinetic and potential energy present in ocean waves into electricity [5]. Moreover, their environmental and economic feasibility have also been investigated.

There are several methods for WEC classification. The first one is based on location. The WEC can be located at the shoreline or offshore. Offshore devices can harvest greater amounts of energy. The following criterion is how the device operates; it can be divided into submerged pressure differential, oscillating water column, overtopping device, or oscillating surge wave energy converter [6], which is the most popular one [7]. In this research, an offshore OSWEC device is investigated.

The vigorous surge motion, cost-effective installation, and minimal environmental impact have made OSWECs a preferable choice [8]. Numerous studies have investigated the potential of Oscillating Surge Wave Energy Converters (OSWECs) as a viable wave energy conversion technology; for instance, Ghasemipour et al. inspected nearshore regions of the southern coast of Iran for the feasibility of such devices [9]. Folley et al. have studied the effects of water depth [10] and device width [11] on the performance of OSWECs. The effects of the device's flap's width [12], length [13], orientation [14], shape, weight, and thickness [15] on the converter's performance have also been studied. It's been shown that the increase in the OSWEC's PTO has positive effects on power and flap's motion amplitude up to a certain point [16]. The wave characteristics like frequency [11] and period [17] can also influence the OSWEC's performance. Moreover, Lin et al. showed that, on average, the viscous loss of the fluid decreases the capture factor by 20% [18].

Almost all the numerical simulations in recent years have been based on Computational Fluid Dynamics (CFD). On one end of the spectrum of these methods is the Linear Potential Flow theory models [19], which are fast but not very accurate. On the other hand, some studies [20, 21] have used Reynolds Averaged Navier–Stokes Equations (RANS) CFD solvers for WEC analysis and simulation, which are computationally complex and slow but offer higher fidelity [22]. Recently, the WEC-Sim module, designed for MATLAB and LPF-based, has been extensively used for WEC simulations [23]. Different types of converters like point absorbers [24], OSWECs [25, 26, 27, 28], FOSWECs [29, 30, 31], and even novel WEC types [32] have been inspected using WEC-Sim. WEC-Sim is an open-source simulation tool designed for WEC numerical simulations [33]. Much research has been utilizing WEC-Sim to investigate OSWEC performance, which encompasses a variety of objectives, for instance, minimizing cost [25], reducing the hydrodynamic loads [34], lowering the applied loads to the support structure of the device [26], and mitigating the horizontal motion of the OSWEC's platform which in turn reduces costs [31]. In the early studies of wave energy converters, the predominant focus of numerical studies was on linear PTOs. For instance, Sheng et al. have optimized two models of linear PTOs for a Wave-Activated Bodies WEC [35] and an OWC [36]. However, researchers have since shown interest in the performance analysis of WECs with a Hydraulic PTO [37, 38, 39].

A variety of optimization studies have also been used in this field. In [40], an improved version of the differential evolution (DE) algorithm was used for a WEC array, simultaneously achieving more precise convergence and speed. Gomes et al. [41] did a hull optimization of a floating OWC using DE and COBYLA, a direct search method to achieve maximum power output. The Genetic Algorithm (GA) has been used widely in the field of wave energy generation; for instance, in [42], it has been used for shape optimization of a planar pressure differential WEC, and in [43], the WEC array configuration was optimized as well.

In [44], multiple meta-heuristic optimization algorithms, like GA or Particle Swarm Optimization (PSO), were used for the geometry optimization of WECs. The PSO has also been used for the optimization of WEC systems [45, 46]. Furthermore, Neshat et al. devised the improved Moth-Flame Optimizer (MFO) to optimize the geometry and the PTO settings of a generic multi-mode WEC [47]. Moreover, the GWO has been utilized for optimization in the field of other sources of renewable energy as well [48, 49].

This study proposes a fast and effective hybrid optimization method for maximizing the power absorption of an OSWEC based on the hindcast wave data from nine zones in the Caspian Sea, each has 9-12 data points. The significant contributions of this work are as follows:

- Proposing a novel optimizer to maximize the power absorption of an OSWEC, the Hill Climb-Explorative Gray Wolf Optimizer (HC-EGWO) methodology combines a local search method with a global optimizer to balance exploration and exploitation rates for improved solution quality.
- Developing a technical feasibility landscape analysis utilizing the Wave Energy Converter Simulator (WECSim) numerical model to account for the maximum feasible angular motion of the flap, ensuring optimized OSWEC operation within safety and efficiency limits.
- Insights for selecting optimal offshore sites, optimizing power output, and promoting the adoption of ocean renewable energy sources.
- Achieving a significant increase in power output (up to 3.31%) compared to other methods demonstrates the effectiveness of the proposed HC-EGWO optimization approach.
- Gaining valuable knowledge for deploying OSWECs in the South Caspian Sea, considering its unique environmental conditions and energy potential.

This study is organized as follows. In section 2, the data collection, WEC's feasibility, and other preliminary analyses are presented. Section 3 goes over the multiple modifications of GWO and proposes a new optimization algorithm. The following section provides the benchmark functions used to evaluate the new algorithm's performance. Section 5 presents the problem formulation information. Finally, Section 6 provides the results of the study.

2. Case Study Landscape Analysis

In this study, both the analytical model and the GWO algorithm were utilized for numerical modeling. The equations in each section were formulated and implemented in MATLAB. Subsequently, the solutions obtained from the proposed optimization approach were duly validated.

2.1. The Caspian Sea

The Caspian Sea is between Iran to the south, Russia to the north, Russia and Azerbaijan to the west, and Turkmenistan and Kazakhstan to the east. This body of water is often categorized either as the largest lake in the world or the most miniature sea on Earth. It spans approximately 1030-1200 kilometers in length and 196-435 kilometers in width. The surface of the Caspian Sea lies around 28 meters below sea level. The northern part of the sea is notably shallow, with only a negligible portion of seawater present in the northern quarter and an average depth of less than 5 meters [50]. Hence, investigating the southern shores becomes more significant for wave analysis. Figure 1 provides an overview of the Caspian Sea. Due to its status as one of Asia's most crucial energy sources, the Caspian Sea has always attracted considerable attention from the industry. The expansion of its southern coast also presents significant potential for harnessing wave energy [51, 52].

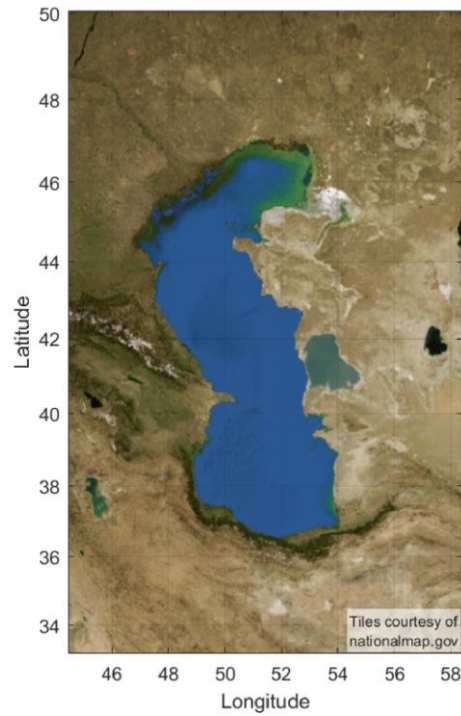


Figure 1: Caspian Sea landscape [50]

Various analyses have been conducted to forecast waves in the southern areas of the Caspian Sea, considering the prevailing direction of the dominant sea waves. Figure 2 displays the projected values of 50-year dominant waves in the southern regions, utilizing the Gumble distribution. Given the wave heights depicted in Figure 2, it becomes crucial to identify a point with maximum wave energy that also offers convenient beach access. Therefore, comprehensive research is needed to analyze wave data in the southern Caspian Sea, aiming to identify this point and establish a general criterion for comparing energy levels among different points using parameters such as wave height and wave period.

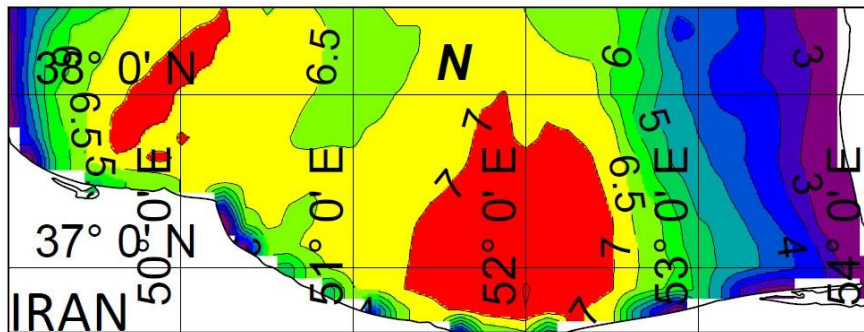


Figure 2: the 50-year design wave height in the dominant directions of the southern Caspian Sea [53]

2.2. Data Collection

To investigate the southern coasts of the Caspian Sea, the initial step involved analyzing the data obtained from the Iranian National Institute for Oceanography and Atmospheric Science (INIO). Specifically, the applied data from the Iranian Seas Wave Modeling (ISWM) and the Iranian Wave Atlas (IWA) models were examined. These datasets covered the entire Caspian Sea over a five-year period, from January 2006 to December 2010, with 1-hour time

intervals. With reference to relevant literature and local assessments, nine ports were selected on the southern coasts of the Caspian Sea. A designated area of 0.2 longitude and latitude was considered around these ports, and locations with available data within this area were extracted. In total, 105 data points from the southern coast area of the Caspian Sea were identified, and their specifications are detailed in Figure 3 and Figure 4.

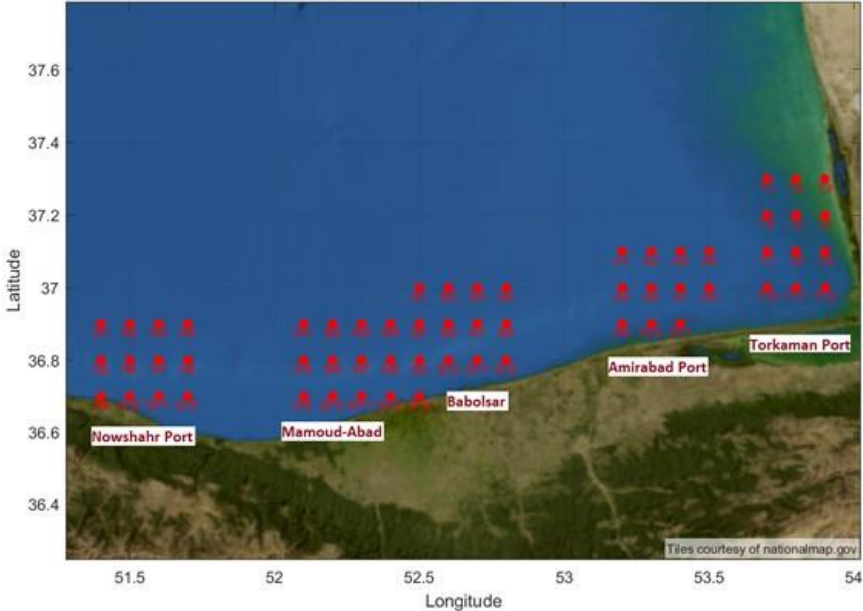


Figure 3: A representation of the surveyed areas along the southeastern coast of the Caspian Sea, including Torkaman, Amirabad, Babolsar, Mahmoud-Abad, and Nowshahr Port.

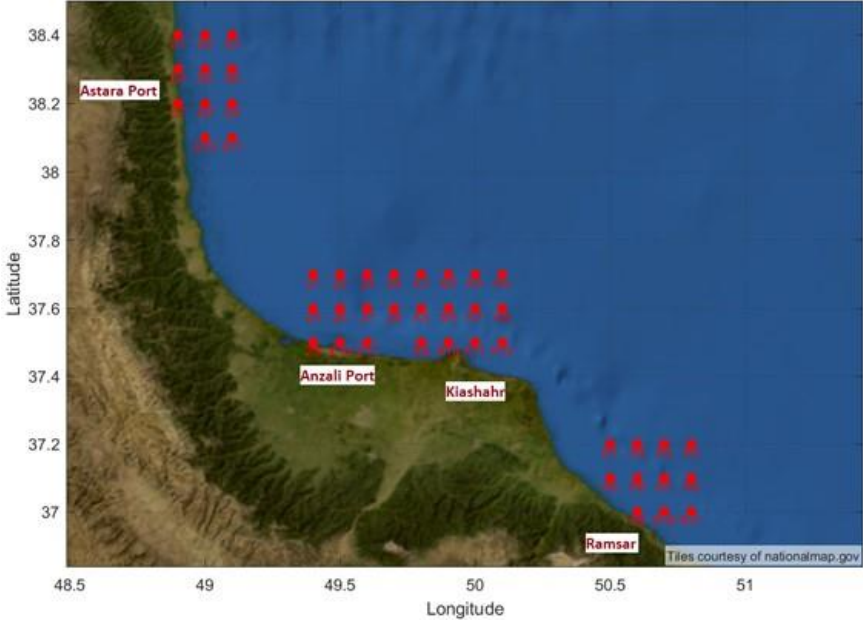


Figure 4: A representation of the surveyed areas along the southeastern coast of the Caspian Sea, including Ramsar, Kiashahr, Anzali Port, and Astara Port.

2.3. Preliminary Analysis

In order to understand the waves in the Caspian Sea, the data from nine selected ports were visualized. This was done by plotting wave rose diagrams (Figure 5) and wave scatter diagrams (Figure 6) to visualize the distribution of wave directions and to identify the prevailing wave patterns in the region. The variations in wave height and wave period across different locations in the study area were unveiled by analyzing the wave scatter diagrams. As seen in Figure 5, the waves have a relatively small magnitude and are mainly to the north, which is logical because these ports are in the southern part of the Caspian Sea. Moreover, from the scatter wave diagram in Figure 6, the waves comparably have low heights and low periods, and the most prevalent waves have a height of 20 cm and a period of 3 seconds.

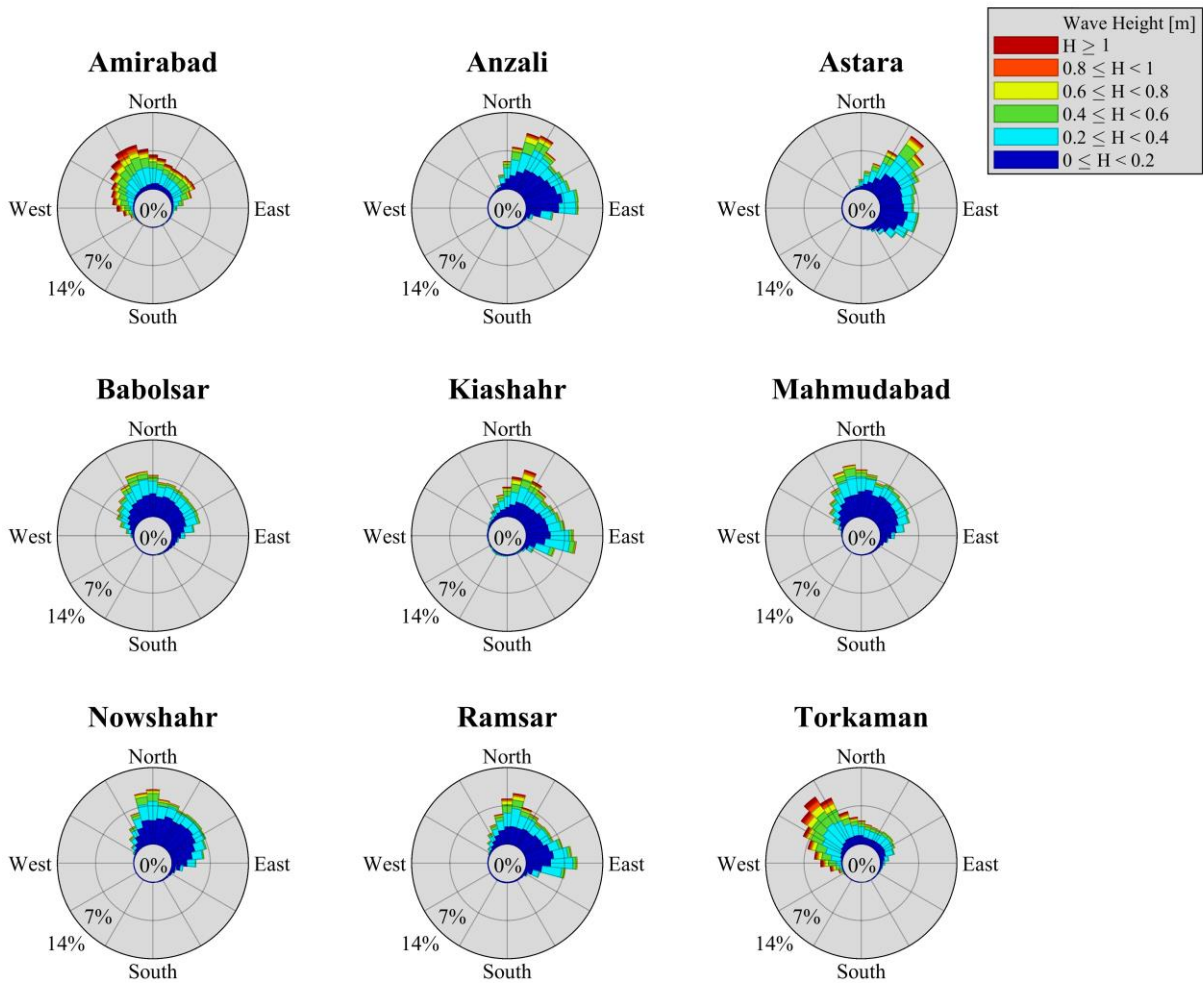


Figure 5: the wave rose diagram for the nine analyzed sea ports reveals relatively small wave magnitudes that predominantly originate from the north. This observation aligns with expectations since these ports are located in the southern region of the Caspian Sea.

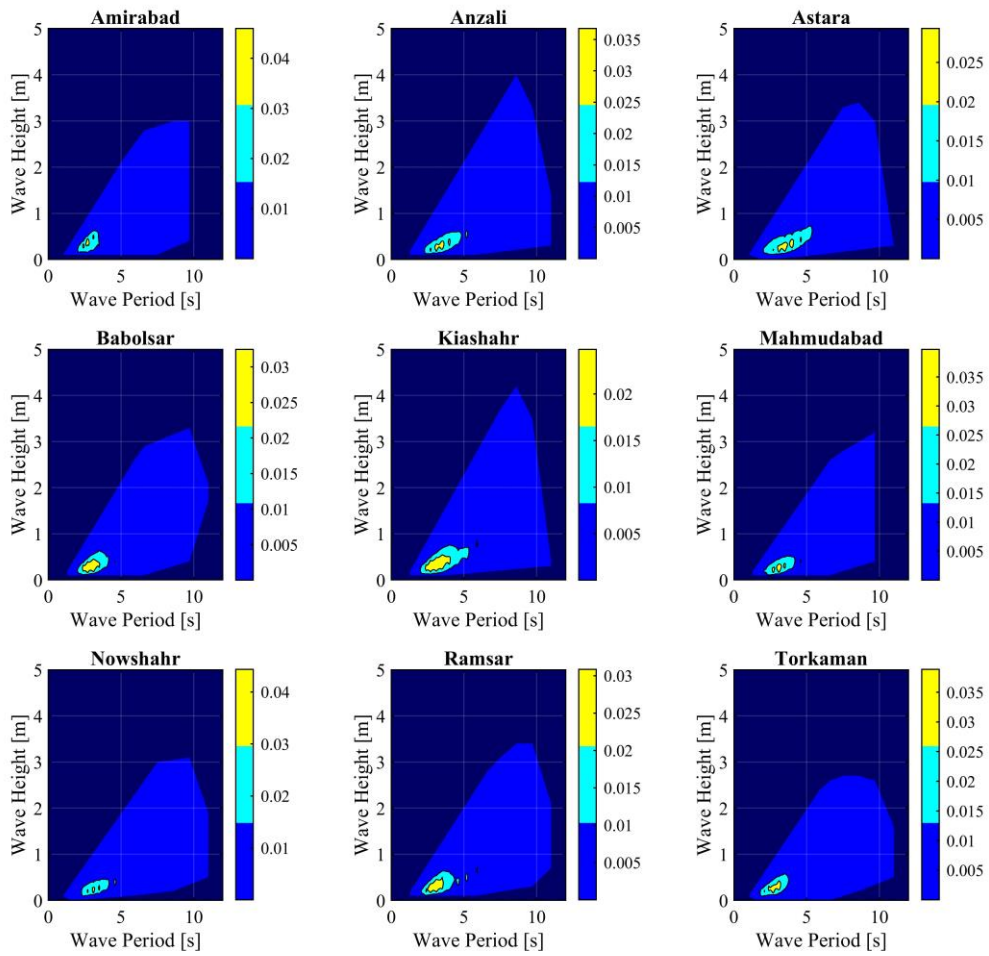


Figure 6: The wave scatter diagram of the nine studied ports.

A power matrix was also made specifically for the Caspian Sea, shown in Figure 7. This matrix comprehensively assessed the wave energy potential in these regions. It takes into account important factors such as wave height and wave period to estimate the energy conversion capabilities of OSWECs in these areas. As shown in Figure 7, increasing either the height or the period of the wave can lead to higher absorbed energy.

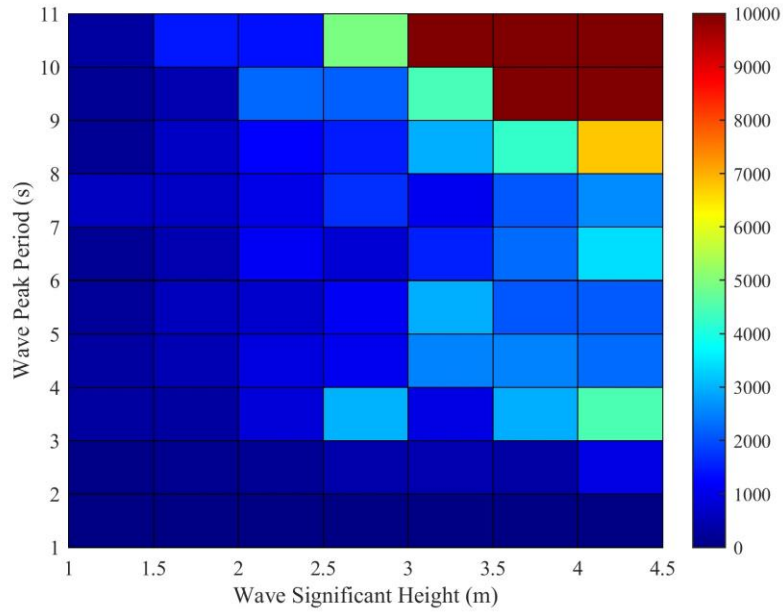


Figure 7: The power matrix of the southern coasts of the Caspian Sea.

Collectively, the insights gained from the wave rose diagrams, wave scatter diagrams, and power matrix contribute to our understanding of the spatial distribution of wave energy in the Caspian Sea.

2.4. WEC's Feasibility

Analysis of OSWEC's flap interaction with the wave under linear water wave theory assumptions requires the flap's excursions to be adequately small. The reason is that the flap's rotation should be small enough so that the correct and non-linear form of the hydrostatic stiffness, which is $(K_p \sin\theta)$, can be replaced by (K_p) [54]. Several studies [55, 17, 56, 16, 57] assumed the maximum angular motion of the flap to be 30° [55]. In addition, this limitation helps the device to avoid damage, particularly in extreme sea states [56]. In Figure 8, the feasible area of the damping and stiffness of the PTO are presented. First, the literature for the range of viable damping and stiffness values for the PTO was reviewed, the result of which is shown by the orange color. Next, based on the OSWEC's flap oscillation limitation, the feasible values of K_{PTO} and C_{PTO} were finalized, and the red area was omitted. Finally, the remaining area, shown by the color green, represents the applicable range of these two critical parameters.

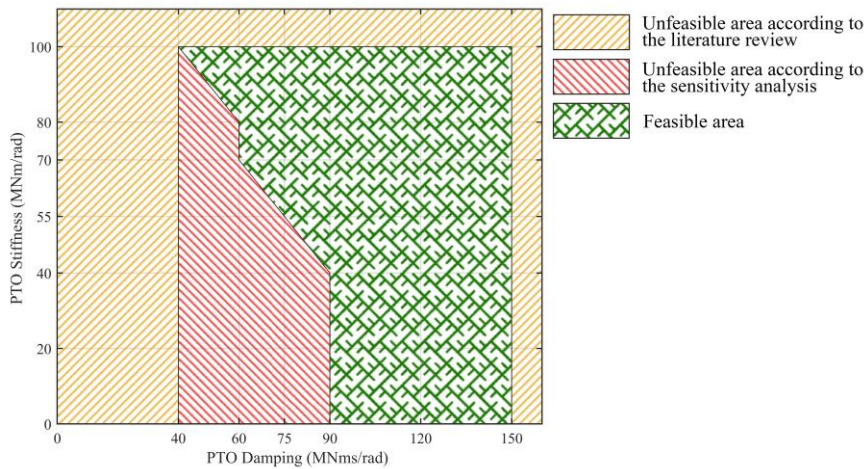


Figure 8: The feasible area of the PTO damping and stiffness used in this study.

2.5. Preliminary Sensitivity Analysis

In order to investigate the impact of critical parameters on the performance of an oscillating wave energy converter, a sensitivity analysis was conducted. Wave height (H), wave period (T), PTO's damping (C), and stiffness (K) were analyzed regarding the power output of the system through six plots in Figure 9. By examining the plots, valuable insights were obtained regarding the optimal values for these parameters and their combinations for maximizing power generation.

Figure 9-(a) represents the effect of H and T in optimizing the generated power of the OSWEC. The plot reveals that a combination of high wave height and wave period leads to the best power outputs. However, it is noteworthy that extreme values of T can decrease the power. Figure 9-(b) illustrates the influence of K and H on the converter's power generation. As can be seen, both high and low levels of PTO stiffness can result in passable power outputs. However, the highest power is achieved when K is moderate. Figure 9-(c) depicts the relation between C and H and the device's generated power. High wave heights and low values of PTO damping correspond to favorable power outputs and improved performance.

Figure 9-(d) shows the effects of K and T variation on power. Accordingly, the wave periods within the range of approximately 6 to 9 seconds yield pleasing power outputs. Furthermore, the power improves significantly as the PTO stiffness approaches its medium value. Figure 9-(e) showcases the influence of C and T . Similar to the previous plot, wave periods ranging from approximately 6 to 9 seconds produce the most favorable power outputs—additionally, the performance improves as the PTO damping decreases. Finally, in Figure 9-(f), the PTO parameters regarding their effect on the power output have been investigated. According to the plot, almost always lower values C result in better power, and a K value between 10 and 70 MNm/rad leads to the best performance. Overall, the parameter's effects can be explained relatively simply. In summary, higher H and lower C lead to the best power outputs. Furthermore, moderate values of T and K lead to the best performance. Overall, it can be seen that the problem at hand is a multimodal optimization problem and has multiple optima.

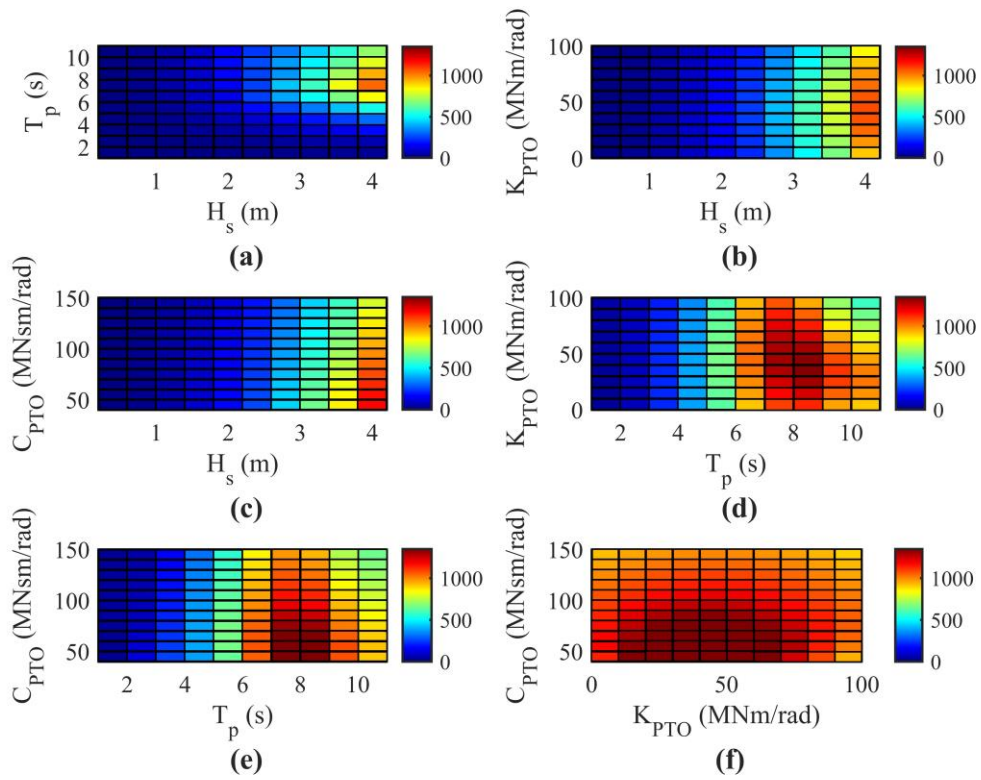


Figure 9: Sensitivity analysis plots for the key parameters of the OSWEC (Wave height, wave period, PTO damping, and PTO stiffness)

Next, the effects of the PTO parameters on the PTO power were further inspected in Figure 10. The black parts show the unfeasible areas calculated in previous sections. Similar to the power output, low values of C and moderate K values bring about the highest PTO forces. It is worth noting that in the OSWEC, the power output is calculated by multiplying PTO force by the flap's velocity [17].

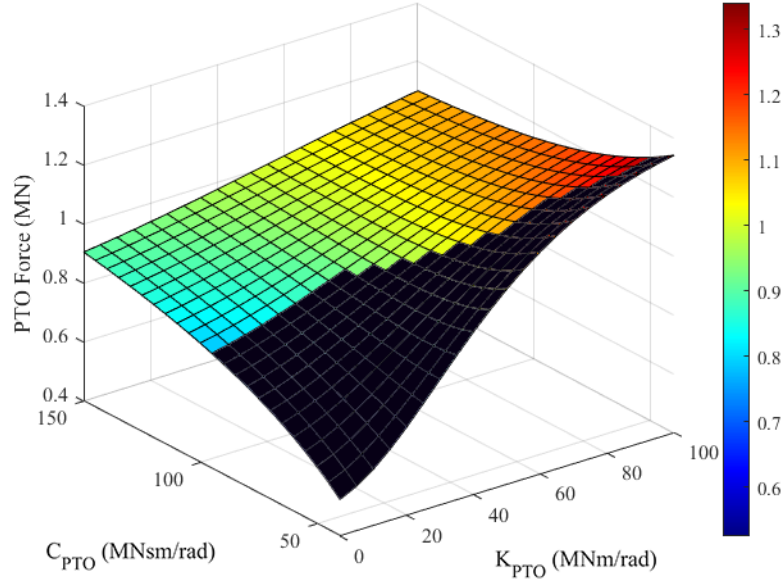


Figure 10: Sensitivity analysis result of the effects of PTO parameters on the PTO force. Unfeasible values, shown in black, are excluded from the analysis.

3. Optimization Approach

3.1. The Standard GWO

The Grey Wolf Optimizer (GWO) is a bio-inspired algorithm based on a grey wolf breed's leadership hierarchy and hunting behaviour. Mirjalili et al. [58] simplified their hunting mechanism and introduced four types of wolves, the alpha (α), the beta (β), the delta (δ), which are, respectively, the best solutions of the algorithms (have the best knowledge about the location of the optimum) and the omegas (ω) which comprise the rest of the pack and follow the three aforementioned wolves to get closer to the prey.

We can show the encircling of the prey process mathematically using the following equations:

$$\vec{D} = |\vec{C} \cdot \vec{X}_p(t) - \vec{X}(t)| \quad (1)$$

$$\vec{X}(t+1) = \vec{X}_p(t) - \vec{A} \cdot \vec{D} \quad (2)$$

in which t is the current iteration, \vec{X} indicates the position of a grey wolf, \vec{X}_p is the position of the prey, and \vec{A} and \vec{C} are coefficient vectors. The \vec{A} and \vec{C} vectors are determined as follows:

$$\vec{A} = 2\vec{a} \cdot \vec{r}_1 - \vec{a} \quad (3)$$

$$\vec{C} = 2 \cdot \vec{r}_2 \quad (4)$$

in which \vec{a} linearly decreases from 2 to 0, and \vec{r}_1 and \vec{r}_2 are random numbers between 0 and 1. As stated, the ω wolves update their positions based on the three best search agents (α, β , and δ wolves). They follow these equations:

$$\vec{D}_\alpha = |\vec{C}_1 \cdot \vec{X}_\alpha - \vec{X}| \quad (5)$$

$$\vec{D}_\beta = |\vec{C}_2 \cdot \vec{X}_\beta - \vec{X}| \quad (6)$$

$$\vec{D}_\delta = |\vec{C}_3 \cdot \vec{X}_\delta - \vec{X}| \quad (7)$$

$$\vec{X}_1 = \vec{X}_\alpha - \vec{A}_1 \cdot (\vec{D}_\alpha) \quad (8)$$

$$\vec{X}_2 = \vec{X}_\beta - \vec{A}_2 \cdot (\vec{D}_\beta) \quad (9)$$

$$\vec{X}_3 = \vec{X}_\delta - \vec{A}_3 \cdot (\vec{D}_\delta) \quad (10)$$

$$\vec{X}(t+1) = \frac{\vec{X}_1(t) + \vec{X}_2(t) + \vec{X}_3(t)}{3} \quad (11)$$

This was a simple overview of GWO's origin and mechanism.

3.2. Modified GWO (mGWO)

Mittal et al. [59] believed that the linear equation of the a does not provide a good balance between exploration and exploitation, so they tried this nonlinear equation:

$$\vec{a} = 2 \left(1 - \frac{t^2}{T^2} \right) \quad (12)$$

in which t represents the current iteration, and T is the total number of iterations. This equation resulted in 70% exploration and 30% exploitation of the total iterations.

3.3. Exploration-Enhanced GWO (EEGWO)

Since in GWO, all the search agents gravitate toward the three best solutions, this algorithm can be susceptible to premature convergence. Therefore, Long et al. [60] modified the position-updating equation inspired by the PSO algorithm to emphasize more on the exploration:

$$\vec{X}(t+1) = b_1 \cdot r_3 \cdot \frac{\vec{X}_1(t) + \vec{X}_2(t) + \vec{X}_3(t)}{3} + b_2 \cdot r_4 \cdot (\vec{X}^i - \vec{X}) \quad (13)$$

where \vec{X}^i is another randomly selected search agent from the population, r_3 and r_4 are random numbers in $[0,1]$, and $b_1, b_2 \in (0,1]$ indicate constant coefficients to balance the exploration/exploitation (in the mentioned study the selected values are $b_1 = 0.1$ and $b_2 = 0.9$).

They also proposed a new formula for the control parameter \vec{a} :

$$\vec{a} = a_{\text{initial}} - (a_{\text{initial}} - a_{\text{final}}) \cdot \left(\frac{T-t}{T} \right)^\mu \quad (14)$$

where μ is the nonlinear modulation index ($\mu = 1.5$ in the aforementioned study), and a_{initial} and a_{final} are 2 and 0, respectively.

3.4. Improved GWO (IGWO)

In order to address the challenges associated with the conventional Maximum Power Point Tracking (MPPT) techniques, which is the power maximization of the PV system [61], and improving their efficiency in finding the global maximum power point, Ma et al. [62] utilized the fitness value of the search agents for their position-updating mechanism as follow:

$$\vec{X}(t+1) = \begin{cases} \frac{f_{\alpha} \cdot \vec{X}_1}{f} + \frac{f_{\beta} \cdot \vec{X}_2}{f} + \frac{f_{\delta} \cdot \vec{X}_3}{f}, \\ \frac{\vec{X}_1 + \vec{X}_2 + \vec{X}_3}{3}, \end{cases} \quad (15)$$

$$f = f_{\alpha} + f_{\beta} + f_{\delta} \quad (16)$$

where f_{α} , f_{β} , and f_{δ} are fitness values of α , β , and δ , respectively. f_{avg} is the average of these 3 fitness values, and f_i is the fitness value of grey wolf individuals.

The authors modified the \vec{a} formula as well:

$$\vec{a} = a_{\text{min}} + (a_{\text{max}} - a_{\text{min}}) \cdot \left(1 - \frac{t}{T}\right)^2 \quad (17)$$

where a_{min} and a_{max} are 0 and 2, respectively.

3.5. Efficient and Robust GWO (ERGWO)

With the intention of tackling large-scale numerical optimization problems, Long et al. performed another study to enhance the performance of the GWO [63]. Following the footsteps of the previous studies, they changed both the position-updating equation and a equation. The first change can be seen below, where they used a proportional weighting method similar to [62]:

$$w_1 = \frac{|\vec{X}_1|}{|\vec{X}_1| + |\vec{X}_2| + |\vec{X}_3|} \quad (18)$$

$$w_2 = \frac{|\vec{X}_2|}{|\vec{X}_1| + |\vec{X}_2| + |\vec{X}_3|} \quad (19)$$

$$w_3 = \frac{|\vec{X}_3|}{|\vec{X}_1| + |\vec{X}_2| + |\vec{X}_3|} \quad (20)$$

$$\vec{X}(t+1) = \frac{1}{w_1 + w_2 + w_3} \cdot \frac{w_1 \cdot \vec{X}_1 + w_2 \cdot \vec{X}_2 + w_3 \cdot \vec{X}_3}{3} \quad (21)$$

where a_{initial} and a_{final} are 2 and 0, respectively. $\mu \in [1.0001, 1.005]$ is the nonlinear modulation index (in the mentioned study $\mu = 1.001$).

$$\vec{a} = a_{\text{initial}} - (a_{\text{initial}} - a_{\text{final}}) \cdot \mu^{-t} \quad (22)$$

3.6. Hill-Climbing Exploraitve GWO (HC-EGWO)

The Gray Wolf Optimizer (GWO), although remarkable in its performance for solving diverse optimization problems [58], is not without its shortcomings. Primarily, it is prone to premature convergence towards local optima in the search space, specifically during complex, high-dimensional problems [64]. This challenge arises due to the declining exploration rate (parameter a) in the original GWO algorithm, which transitions from 2 to 0 linearly. While this allows the algorithm to either explore or exploit optimal solutions when a is above 1, it leads to exploitation when a is below 1, thereby accelerating convergence towards local optima.

In addressing this limitation, we propose the Explorative Gray Wolf Optimizer (EGWO), a novel enhancement to the original GWO that amplifies the exploration rate by modifying the parameter a . In EGWO, a is altered as per the equations:

$$R = \left(\frac{T - t}{T - 1} \right) \quad (23)$$

$$\vec{a} = 2 \cdot \left(1 - \left(e^{(t^R - T^R)} \right) \right) \quad (24)$$

where t is the current iteration, and T is the maximum number of iterations. This modification empowers the algorithm to delay the convergence process and explore the search space more thoroughly, reducing the chance of being trapped in local optima. Furthermore, to fortify the global search capabilities of EGWO, we propose a robust hybrid algorithm that incorporates a Random-restart hill-climbing local search, dubbed HC-EGWO. Figure 11 shows the evolution of a throughout the iterations for each of the six optimization approaches. Also, the Exploration Ratio (ER) is presented for each method; this value shows how much of the search process is allocated to potential exploration in GWO. By comparing the values, it is clear that HC-EGWO has the best ER value and the most potential to search the unexplored areas of the search space thoroughly.

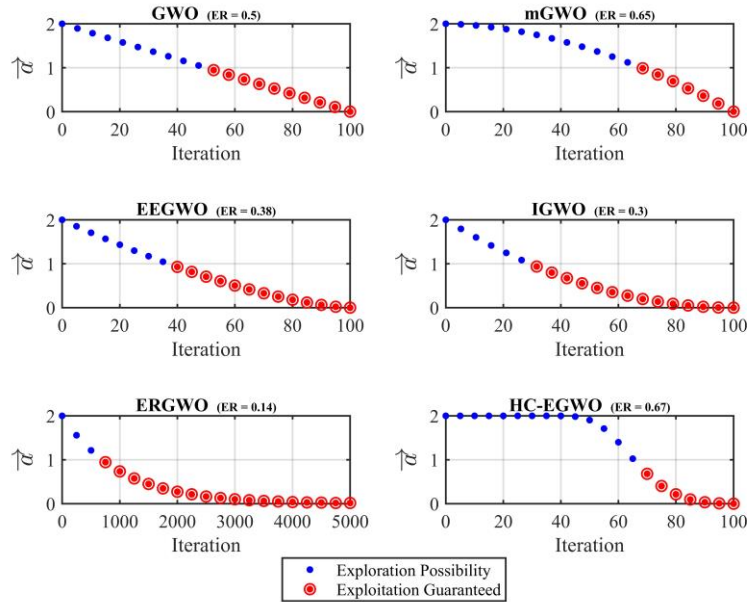


Figure 11: The evolution of a value during the optimization process for the six evaluated GWO methods in this study, and their Exploration Ratio (ER)

In this hybrid scheme, EGWO operates on a superior level to create a global track and procure an array of suitable solutions. When the EGWO encounters stagnation or converges prematurely towards a local optimum, the hill climbing algorithm initiates a local search around the best solution found by the upper level (EGWO). It does so by creating a comprehensive neighbourhood search, thereby preparing to escape such unfavourable scenarios.

The performance threshold is computed as follows:

$$\Delta \text{Best}_{THD} = \frac{\sum_{k=1}^M (\text{Best}_{THD}_k - \text{Best}_{THD}_{k-1})}{M} \quad (25)$$

where Best_{THD} is the optimal solution found per generation, and M is tied to the range of iterations to determine the average EGWO performance. When the solution offered by the local search outperforms the initial one, EGWO's global best is updated.

The HC-EGWO algorithm iteratively executes the hill-climbing process whenever the EGWO performance dips, each time establishing an initial condition to facilitate escape from undesirable circumstances. The search step size is decremented linearly as follows to achieve a fine balance between exploration and exploitation:

$$S_t = S_t - \left(\frac{t}{T} S_t\right) + 1 \quad (26)$$

Here, t and T denote the current and maximum iteration numbers, respectively, while S_t represents the neighborhood search's step size.

Algorithm 1 illustrates the detailed steps of the proposed optimization method (HC-EGWO). The initial solution encompasses wave height (H), wave period (T), PTO stiffness coefficient (K), and PTO damping coefficient (C).

One of the crucial parameters in the local search algorithm is g , which signifies the precision of the neighborhood search surrounding the globally optimal solution proposed by EGWO. A smaller step size for HC slows down the convergence speed. However, a larger step size bolsters the exploration capability, possibly at the expense of the exploitation capability, leading to the possibility of skipping over globally optimal or high-potential solution surfaces. For each decision variable, the neighborhood search evaluates two distinct direct searches, either incremental or decremental. After evaluating the generated solutions, the optimal candidate is chosen to iterate the search algorithm. It should be noted that the HC algorithm should not be employed during the initial iteration of the optimization process due to the pronounced tendency for converging to local optima. Moreover, for optimizing large-scale problems, HC may not be a suitable choice.

Algorithm 1 Hill Climbing Explorative Gray Wolf Optimizer

```

1: procedure HC-EGWO
2:    $N = 30, D = 4$  ▷ Population size and dimension size
3:    $\mathbb{S} = \{\langle H_1, T_1, K_1, D_1 \rangle, \dots, \langle H_N, T_N, K_N, D_N \rangle\}$  ▷ Initialize the population of wolves
4:   Check if  $lb_1^N \leq \mathbb{S} \leq ub_1^N$ 
5:    $Max_{iter} = 100$  ▷ Maximum number of iterations
6:   for  $iter = 1, \dots, Max_{iter}$  do
7:      $R = (Max_{iter} - iter) / (Max_{iter} - 1)$ 
8:      $\vec{a} = 2 \cdot (1 - e^{(iter^R - Max_{iter}^R)})$  ▷ Calculate exploration rate  $\vec{a}$  with the new formulation
9:     Sort the population  $\mathbb{S}$  based on fitness and get the leading wolves  $\alpha, \beta$ , and  $\delta$ 
10:    for  $i = 1, \dots, N$  do
11:      for  $j = 1, \dots, D$  do
12:        Calculate  $A_{ij}$  and  $C_{ij}$  for each of the leading wolves
13:        Update the position of the  $i$ th wolf in dimension  $j$  using the positions of  $\alpha, \beta$ , and  $\delta$ 
14:      end for
15:    end for
16:    Update the positions of  $\alpha, \beta$ , and  $\delta$  based on the updated population
17:     $Best_{iter} = \text{Max}(\mathbb{S})$  ▷ Get the best solution in this iteration
18:     $\Delta Best = Best_{iter} - Best_{iter-1}$  ▷ Calculate the difference between the best solutions in the current and previous iterations
19:    if  $\Delta Best < Th$  then ▷ If the difference is less than a threshold  $Th$ , perform Hill Climbing
20:      Initialize the constraints  $lb_1^d, ub_1^d$ 

```



```

21:       $S_1^d = (Min_1^d + Max_1^d)/g$                                 ▶ Compute the step size, g is search resolution
22:       $Sol_1 = \{ \langle H, T, K, D \rangle \}$                                 ▶ Initial solution
23:       $(fitness_1) = Eval(Sol_1)$                                 ▶ Evaluate the solution
24:      for  $iter \leq Max_{iter}$  do
25:           $Te = Sol_{iter}$ 
26:          while  $t \leq len(Sol_1)$  do
27:               $Te_t = Te_t \pm S_t$                                 ▶ Neighborhood search
28:               $(fitness_t^{iter}) = Eval(Te_t)$ 
29:               $t = t + 1$ 
30:          end while
31:           $\langle Max_{fit}, Index_{max} \rangle = Max(fitness)$ 
32:           $Sol_{iter} = Te_t(Index_{max})$                                 ▶ Select the best feasible solution and update the design
33:           $S_t = S_t - (\frac{iter}{Max_{iter}} S_t) + 1$                                 ▶  $S_t$  linearly reduced
34:      end for
35:       $Best_{iter} = Sol_{iter}$ 
36:  end if
37:  end for
38:  return  $Best_{iter}$                                 ▶ Return the best solution
39: end procedure

```

4. Benchmark Functions

In this section, we evaluate the performance of the HC-EGWO algorithm on a total of 16 benchmark functions. These are classical benchmark functions that have been widely used by researchers in the field. These functions are well-established and are commonly used to evaluate the performance of optimization algorithms. You can find a detailed list of these classical benchmark functions in Tables 1 and 2. The tables provide information such as the dimensionality (Dim) of the function, the range of the function's search space (Range), and the optimal value (fmin) of each function [58]. By benchmarking the HC-EGWO algorithm on these 16 functions, we can evaluate its performance and compare it to other optimization algorithms.

All the benchmark functions employed in this study are aimed at minimizing a given objective. These functions can be classified either as multimodal or fixed-dimension multimodal. To assess the performance of the HC-EGWO, it was executed 30 times on each benchmark function. The results were then analyzed statistically, providing the average and standard deviation values. These statistical outcomes are presented in Tables 5, which allow for comparing and evaluating the algorithm's performance across the benchmark functions. Also, a statistical analysis of the comparison is presented in the results section. To validate the results, the HC-EGWO algorithm is compared against other variations of the GWO algorithm, namely the conventional Grey Wolf Optimizer [58], the modified GWO [59], the Exploration-Enhanced GWO [60], the Improved GWO [62], and the Efficient and Robust GWO [63].

Table 1: Multimodal Benchmark Functions [58]

Function	Dim	Range	f_{min}
$F_1(x) = \sum_{i=1}^n (-x_i \cdot \sin(\sqrt{ x_i }))$	30	[-500, 500]	-418.9829x5
$F_2(x) = \sum_{i=1}^n (x_i^2 - 10 \cdot \cos(2\pi x_i) + 10)$	30	[-5.12, 5.12]	0
$F_3(x) = -20 \cdot \exp\left(-0.2 \cdot \sqrt{\frac{\sum_{i=1}^n x_i^2}{n}}\right) - \exp\left(\frac{1}{n} \sum_{i=1}^n \cos(2\pi x_i)\right) + 20 + e$	30	[-32, 32]	0
$F_4(x) = \frac{1}{4000} \sum_{i=1}^n x_i^2 - \prod_{i=1}^n \cos\left(\frac{x_i}{\sqrt{i}}\right) + 1$	30	[-600, 600]	0
$F_5 = \frac{\pi}{n}(10 \sin(\pi y_1)) + \sum_{i=1}^{n-1} (y_i - 1)^2 \cdot (1 + 10 \sin^2(\pi y_{i+1})) + (y_n - 1)^2 + \sum_{i=1}^n u(x_i, 10, 100, 4)$	30	[-100, 100]	0
$y_i = 1 + \frac{x_i + 1}{4}$ $u(x_i, a, k, m) = \begin{cases} k(x_i - a)^m & x_i > a \\ 0 & -a < x_i < a \\ k(-x_i - a)^m & x_i < -a \end{cases}$			
$F_6(x) = 0.1 \left(\sin^2(3\pi x_1) + \sum_{i=1}^n ((x_i - 1)^2 \cdot (1 + \sin^2(3\pi x_i + 1))) \right) + (x_n - 1)^2 (1 + \sin^2(2\pi x_n)) + \sum_{i=1}^n U(x_i, 5, 100, 4)$	30	[-50, 50]	0

Table 2: Fixed-dimension Multimodal Benchmark Functions. [58]

Function	Dim	Range	f_{min}
$F_7 = \left(\frac{1}{500} + \sum_{j=1}^{25} \frac{1}{j + \sum_{i=1}^2 (x_i - a_{ij})^6} \right)^{-1}$	2	[-65, 65]	1
$F_8(x) = \sum_{i=1}^{11} \left(a_i - \frac{x_1(b_i^2 + x_2 b_i)}{b_i^2 + x_3 b_i + x_4} \right)^2$	4	[-5, 5]	0.00030
$F_9(x) = 4x_1^2 - 2.1x_1^4 + \frac{1}{3}x_1^6 + x_1x_2 - 4x_2^2 + 4x_2^4$	2	[-5, 5]	-1.0316
$F_{10}(x) = \left(x_2 - \frac{5.1}{4\pi^2}x_1^2 + \frac{5}{\pi}x_1 - 6 \right)^2$ $+ 10 \left(1 - \frac{1}{8\pi} \right) \cos(x_1) + 10$	2	[-5, 5]	0.398
$F_{11}(x) = \left(1 + (x_1 + x_2 + 1)^2(19 - 14x_1 + 3x_1^2 - 14x_2 + 6x_1x_2 + 3x_2^2) \right)^2 \left(30 + (2x_1 - 3x_2)^2(18 - 32x_1 + 12x_1^2 + 48x_2 - 36x_1x_2 + 27x_2^2) \right)$	2	[-2, 2]	3
$F_{12}(x) = -\sum_{i=1}^4 \left(c_i \exp \left(-\sum_{j=1}^3 a_{ij}(x_j - p_{ij})^2 \right) \right)$	3	[1, 3]	-3.86
$F_{13}(x) = -\sum_{i=1}^4 \left(c_i \exp \left(-\sum_{j=1}^6 a_{ij}(x_j - p_{ij})^2 \right) \right)$	6	[0, 1]	-3.32
$F_{14}(x) = -\sum_{i=1}^5 \left(\left((X - a_i)(X - a_i)^T + c_i \right)^{-1} \right)$	4	[0, 10]	-10.1532
$F_{15}(x) = -\sum_{i=1}^7 \left(\left((X - a_i)(X - a_i)^T + c_i \right)^{-1} \right)$	4	[0, 10]	-10.4028
$F_{16}(x) = -\sum_{i=1}^{10} \left(\left((X - a_i)(X - a_i)^T + c_i \right)^{-1} \right)$	4	[0, 10]	10.5363

5. Problem Formulation

5.1. The Wave Energy Converter

As stated before, the Oscillating Surge WEC was chosen for this study due to multiple reasons. The OSWEC is fixed to the ground, and it features a hinged connection between its base and flap. This hinge constrains the flap's movement, allowing it to pitch around the hinge point. The converter's physical dimensions at scale are shown in Figure 12. Moreover, the OSWEC's flap has a mass of 127 tonnes, and its other properties are listed in Table 3.

Table 3: OSWEC's Flap Mass Properties [23]

Body	Direction	Center of Gravity (m)	I_{xx} (kg.m ²)	I_{yy} (kg.m ²)	I_{zz} (kg.m ²)
Flap	x	0	0	0	0
	y	0	0	1,850,000	0
	z	-3.9	0	0	0

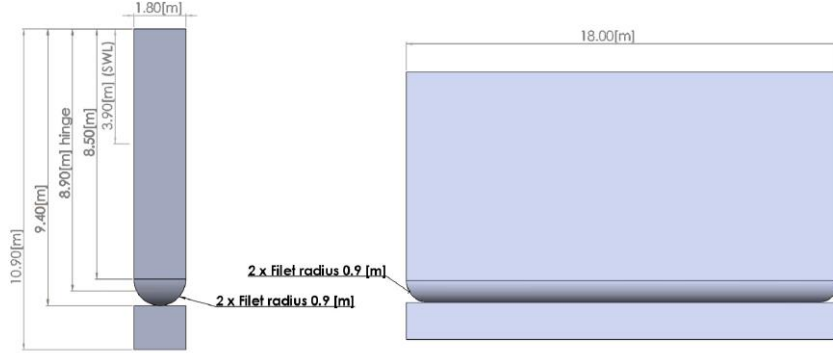


Figure 12: OSWEC's full-scale detailed dimensions [23]

5.2. WEC-Sim

WEC-Sim provides an open-source simulation tool for the community. In order to determine the dynamic response of the WEC system, the equation of motion for the device about its center of gravity in the time domain has to be solved [23]:

$$m\ddot{X} = F_{exc}(t) + F_{rad}(t) + F_{PTO}(t) + F_B(t) \quad (27)$$

where m is the mass matrix of the WEC, X is the acceleration vector, $F_{exc}(t)$ is the wave excitation vector, $F_{rad}(t)$ is the force and torque vector caused by wave radiation, $F_{PTO}(t)$ is the PTO force and torque vector, and $F_B(t)$ is the net buoyancy restoring force and torque vector. The $F_{exc}(t)$ and $F_{rad}(t)$ are calculated using Boundary Element Method (BEM) solvers [65]. This module is developed on MATLAB/Simulink/Simscape. Figure 13 shows the Simulink models of the proposed OSWEC investigated in this paper [23]. Moreover, irregular waves are simulated as a superposition of regular waves [66].

In WEC-Sim, the PTO unit can be characterized by a linear spring-damper system, in which the PTO force is calculated by:

$$F_{PTO} = K \cdot X + C \cdot X' \quad (28)$$

where K is the PTO stiffness coefficient, C is the PTO damping coefficient, and X and X' are the relative motion and velocity between the flap and the base of the OSWEC. Since the studied device is fixed to the bed, X and X' can be considered the flap's motion and velocity. Next, the power output of the PTO can be obtained by the following [23]:

$$P_{PTO} = F_{PTO} \cdot X' = K \cdot X \cdot X' + C \cdot X'^2 \quad (29)$$

In WEC-Sim, the regular wave excitation force after the ramp time (the necessary time for the system to stabilize from the starting stage of the simulation) is obtained from the:

$$F_{exc}(t) = \Re \left[\frac{H}{2} F_{exc}(\omega, \theta) e^{i\omega t} \right] \quad (30)$$

where \Re denotes the real part of the term in bracket, H is the wave height, F_{exc} is the frequency dependent complex wave-excitation amplitude vector, and θ is the wave direction. The excitation force in irregular sea states can be calculated as follows:

$$F_{exc}(t) = \Re \left[\sum_{j=1}^N F_{exc}(\omega_j, \theta) e^{i(\omega_j t + \phi_j)} \sqrt{2S(\omega_j)} d\omega_j \right] \quad (31)$$

where N is the number of frequency bands that discretizes the wave spectrum, φ is the randomized phase angle, and $S(\omega)$ is the distribution of wave energy over a range of wave frequencies that are characterized by a H_s and T_p .

The software uses the following equation to calculate the radiation terms, namely the added mass and the radiation damping torques. In this equation, the first term is the added mass torque, and the second term is the radiation-damping torque:

$$F_{rad}(t) = -A_{\infty}\ddot{X} - \int_0^t K_r(t - \tau)\dot{X}(\tau)d\tau \quad (32)$$

where A_{∞} is the added mass matrix at an infinite frequency, and K_r is the radiation impulse response function, which is calculated by this equation:

$$K_r t = \frac{2}{\pi} \int_0^{\infty} B(\omega) \cos(\omega t) d\omega \quad (33)$$

Notably, the assumption is that there is no motion before $t = 0$. The A_{∞} and $B(\omega)$ coefficients are calculated by the NEMOH, the BEM solver WEC-Sim uses.

5.3. Optimization Run Details

In order to optimize the performance of an OSWEC in the southern Caspian Sea, WEC-Sim was used to simulate the converter and HC-EGWO to optimize its power output. A simulation time of 400 s and a ramp time of 100 s were chosen, with time steps of 0.1 s. Furthermore, ten optimization runs using HC-EGWO were performed, each with 1000 iterations and 20 search agents.

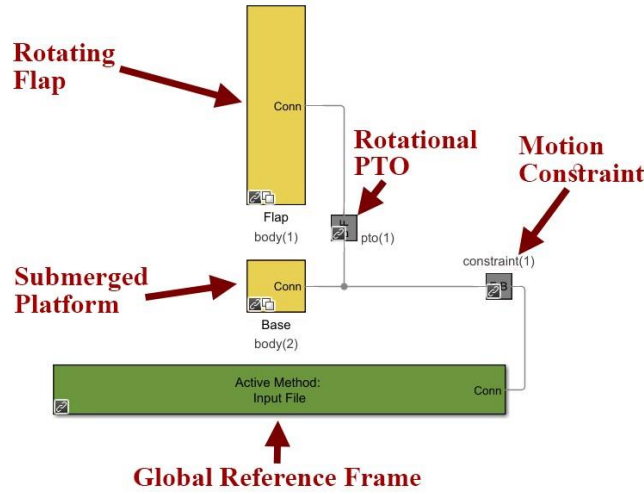


Figure 13: OSWEC's Simulink model in WEC-Sim [23]

Table 4: The details of optimisation parameters and other variables related to the wave power simulation applied.

Abbreviation	Full name	Description
H	Height (m)	Measure of the amplitude or intensity of a wave
T	Period (s)	Time for completing one full cycle of wave
K	PTO Stiffness Coefficient (MNm/rad)	Relationship between the deformation of a PTO system and the force it generates
C	PTO Damping Coefficient (MNsm/rad)	Relationship between the PTO system's velocity and the force it generates
FlapEP	maxFlapExcitationPitch	Maximum Flap's Excitation Force (kN)
FlapRDP	maxFlapRDPitch	Maximum Flap's Radiation Damping Force (kN)
FlapAMP	maxFlapAMPitch	Maximum Flap's Added Math Force (kN)
FlapRP	maxFlapRestoringPitch	Maximum Flap's Restoring Force (kN)
ForceTPTOP	maxForceTotalPTOPitch	Maximum PTO's Force (kN)
meanFlapAVD	meanFlapAngularVelocityD	Average Flap's Velocity (degree/s)
maxFlapAVD	maxFlapAngularVelocityD	Maximum Flap's Velocity (degree/s)
FlapARD	maxFlapAngularRotationD	Maximum Flap's Rotation (degree)
Flapa	flap's acceleration (degree/s ²)	Affects the PTO system's structural integrity & overall performance.
Flapfam	flap's force added math (N)	
Flapfe	flap's excitation force (N)	A function of the displacement, velocity and acceleration of PTO system
Flapfr	flap's restoring force (N)	Result of the buoyancy and gravity forces acting on the WEC
Flapfrd	flap's radiation damping force (N)	Due to the interaction between a WEC and the surrounding water waves
Flapft	flap's total force (N)	Sum of hydrodynamic forces, gravity forces, buoyancy forces, and other forces generated by the PTO system.
Flapv	flap's velocity (degree/s)	Rate of change of the flap angle,
Flapx	flap's position (degree)	
PTOa	PTO's acceleration (degree/s ²)	Alteration rate of its velocity over time
PTOv	PTO's velocity (degree/s)	Alteration rate of its position over time
PTOf	PTO's force (N)	Is transmitted from the WEC to the PTO system due to the motion of the waves
PTOx	PTO's position (degree)	

6. Results

6.1. Benchmark Functions Results

Based on the results of the landscape analysis, it has been revealed that the problem at hand exhibits a multimodal nature. Therefore, multimodal benchmark functions have been used to test the effectiveness of HC-EGWO to optimize a wide range of complex problems. Furthermore, assessing the performance of HC-EGWO using multimodal benchmark functions can help in clarifying the generalization ability of the optimisation method. The importance of generalization lies in its ability to prevent overfitting [67], a situation where an optimization algorithm excessively fine-tunes its parameters to match specific conditions perfectly. Overfitting can result in subpar performance when the algorithm is applied to unfamiliar problem instances. By giving priority to generalization, optimization methods concentrate on capturing fundamental patterns and principles that can be transferred to new problem instances, resulting in solutions that are more dependable and efficient.

These benchmark functions have multiple global and local optima, which increase by the number of dimensions. This characteristic makes them the perfect functions to test the exploration ability of an algorithm [58]. As shown in Table 5, the HC-EGWO can provide very competitive results (especially in fixed-dimension multimodal benchmark function). This algorithm reaches the best solutions in 7 test functions and the second-best answer in 2 functions in this category, which is the best performance among the analyzed algorithms. It is notable that in some functions, like F11 and F12, the difference in performance is very minuscule.

Table 5: Results of the multimodal benchmark functions.

F	GWO		mGWO		EGGWO		IGWO		ERGGWO		HC-EGWO	
	Avg.	Std.	Avg.	Std.	Avg.	Std.	Avg.	Std.	Avg.	Std.	Avg.	Std.
1	-5.792E+03	6.756E+02	-5.347E+03	1.046E+03	-2.096E+03	5.089E+02	-6.054E+03	8.322E+02	-2.202E+03	4.659E+02	-5.743E+03	8.293E+02
2	3.177E+00	3.672E+00	2.842E-14	3.580E-14	0.000E+00	0.000E+00	7.161E+00	4.462E+00	0.000E+00	0.000E+00	1.074E+02	3.002E+01
3	1.007E-13	1.927E-14	2.164E-14	4.324E-15	4.441E-16	0.000E+00	1.977E-09	1.238E-09	3.997E-15	0.000E+00	5.184E-14	1.594E-14
4	4.783E-03	7.820E-03	1.508E-03	4.962E-03	0.000E+00	0.000E+00	9.001E-03	1.102E-02	0.000E+00	0.000E+00	1.718E-03	5.688E-03
5	3.634E-02	1.601E-02	3.843E-02	1.752E-02	1.431E+00	1.188E-01	7.412E-02	5.245E-02	8.409E-01	1.875E-01	5.903E-07	3.399E-07
6	5.820E-01	2.346E-01	5.388E-01	2.066E-01	2.995E+00	1.932E-03	8.668E-01	2.751E-01	2.970E+00	4.908E-02	1.318E-02	3.027E-02
7	5.492E+00	4.853E+00	5.754E+00	4.788E+00	1.161E+01	2.764E+00	5.628E+00	4.552E+00	9.107E+00	3.433E+00	4.721E+00	4.109E+00
8	5.662E-03	1.223E-02	5.664E-03	1.220E-02	1.795E-02	1.400E-02	3.733E-03	7.566E-03	2.822E-03	2.957E-03	2.482E-03	6.065E-03
9	-1.032E+00	1.641E-08	-1.032E+00	7.774E-08	-5.038E-01	2.333E-01	-1.032E+00	2.881E-12	-1.018E+00	1.218E-02	-1.032E+00	5.206E-12
10	3.980E-01	5.884E-04	3.979E-01	3.995E-05	2.550E+00	1.985E+00	3.979E-01	7.629E-11	7.928E-01	3.432E-01	3.980E-01	4.306E-04
11	3.000E+00	4.631E-05	3.000E+00	2.031E-05	6.862E+01	7.135E+01	3.000E+00	6.642E-05	1.012E+01	1.037E+01	3.000E+00	4.306E-04
12	-3.861E+00	2.341E-03	-3.862E+00	2.260E-03	-3.242E+00	4.768E-01	-3.862E+00	2.581E-03	-3.424E+00	3.243E-01	-3.862E+00	1.933E-03
13	-3.279E+00	6.838E-02	-3.281E+00	6.433E-02	-1.601E+00	5.947E-01	-3.278E+00	7.025E-02	-2.003E+00	4.288E-01	-3.241E+00	7.815E-02
14	-8.805E+00	2.541E+00	-9.404E+00	1.949E+00	-7.846E-01	1.940E-01	-9.643E+00	1.556E+00	-2.461E+00	5.867E-01	-9.205E+00	2.190E+00
15	-1.022E+01	9.702E-01	-1.022E+01	9.694E-01	-8.125E-01	2.101E-01	-1.023E+01	9.704E-01	-2.383E+00	7.936E-01	-1.005E+01	1.343E+00
16	-9.814E+00	2.238E+00	-1.008E+01	1.750E+00	-9.005E-01	2.442E-01	-9.790E+00	2.326E+00	-2.470E+00	5.635E-01	-1.054E+01	6.584E-08

Figure 14 shows a comparative plot of the five variants of GWO and the proposed GWO (HC-EGWO) performance over the 16 benchmarks. The performance average rank of each variant and the significant differences using the Friedman test can confirm that HC-EGWO performed best in these 16 multi-modal optimisation benchmarks. The average rank is used to calculate the Friedman statistic, which is compared to the critical value to determine whether there are significant differences in performance.

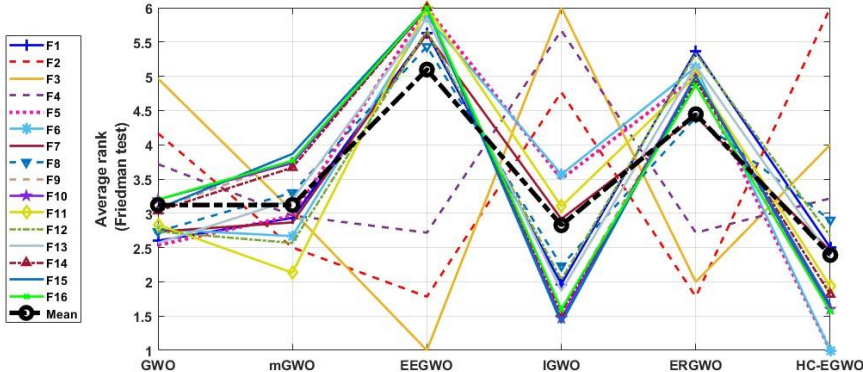


Figure 14: Average performance rank of the HC-EGWO compared with other five variants of GWOs over the 16 benchmarks using the Friedman test.

6.2. Algorithms Performance in the Defined Problem

Here, the proposed algorithm was compared to the conventional GWO and its four variants that were introduced earlier. Each algorithm was run five times with a population size of 20 and 1000 iterations to achieve maximum power output. Table 6 shows the critical parameters of the OSWEC in the average performance of each algorithm.

As can be seen in Table 6, all the algorithms have competitive performances; however, the proposed algorithm (HC-EGWO) outperforms the others. HC-EGWO can improve the power output by 0.08% up to 3.31% compared to the other candidates. Moreover, the EEGWO has the worst performance by far. Next, the convergence curves for the six inspected algorithms are presented in Figure 15.

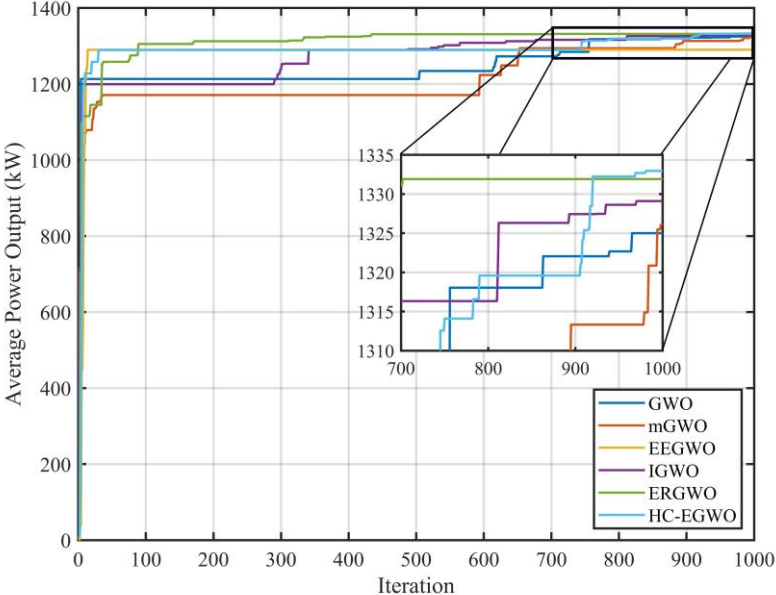


Figure 15: The convergence curves for the average performance of the conventional GWO, its four modifications, and the proposed algorithm in this study.

Figure 15 shows how competitive all these algorithms' performances were in this problem. In addition, all the methods were able to reach high amounts of average power output in under 50 iterations.

6.3. Wave and PTO parameters optimization

In this section, the results of the wave and PTO parameters optimization of the oscillating wave surge converter are presented. In order to get a better understanding of the effects of optimization on performance, the converter's functioning and outputs in 3 scenarios are analyzed and compared. One of the cases is the scenario with the best-found solution by the HC-EGWO (Case C). Next, the case with the default WEC-Sim parameters was chosen to see how much improvement the input fine-tuning has achieved (Case A). However, since the default WEC-Sim case parameters were in the unfeasible area following the literature review this study performed at the research's beginning, another scenario was added for evaluation. It was observed that the PTO damping with a value of 0.012 MNsm/rad was in the unfeasible area, so based on the literature review and the initial sensitivity analysis, the minimum feasible value, which was 90 MNsm/rad, was chosen for the following case, and the three other parameters stayed the same (Case B).

Table 7 presents the inputs, forces, oscillation, and power of the system in the three analyzed cases in detail. First, the wave elevation during the simulation for the 3 cases is presented in Figure 16 in order to analyze the other parameters more effectively.

Next, the resulting oscillation details, PTO force, and power output will be inspected. As stated before, cases A and B have the same wave conditions. Hence, one wave elevation graph is plotted to represent the sea state in both cases in Figure 16. According to this figure, in cases A and B, wave elevation relatively stays in the same range, and the amplitude does not change drastically at any point during the simulation. On the other hand, in case C, especially after the halfway mark, wave heights are greater and reach their maximum absolute value at around the 215-second mark. As previously mentioned, when using linear PTO for the OSWEC, WEC-Sim calculates the power output by multiplying the PTO force by the flap's angular velocity. Both the flap's motion and its angular velocity positively dictate the device's power output, which is this study's main objective.

Table 7: The details of the 3 analyzed cases in this study

	H	T	K	C	FlapEP	FlapRDP	FlapAMP
Case A	2.5	8	0	0.012	1624	1778	691.7
	FlapRP	ForceTPTOP	meanFlapAVD	maxFlapAVD	FlapARD	MaxPower	AvgPower
	887.4	4.158	7.049	19.85	26.29	1.440	0.228
	H	T	K	C	FlapEP	FlapRDP	FlapAMP
Case B	2.5	8	0	90	1624	780.3	297.6
	FlapRP	ForceTPTOP	meanFlapAVD	maxFlapAVD	FlapARD	MaxPower	AvgPower
	360.6	13395	2.733	8.527	10.686	1993	287.7
	H	T	K	C	FlapEP	FlapRDP	FlapAMP
Case C	4.223	7.39	54.46	75.58	3687	1512	722
	FlapRP	ForceTPTOP	meanFlapAVD	maxFlapAVD	FlapARD	MaxPower	AvgPower
	842	38306	3.82	21.92	24.97	13393.98	1332.95

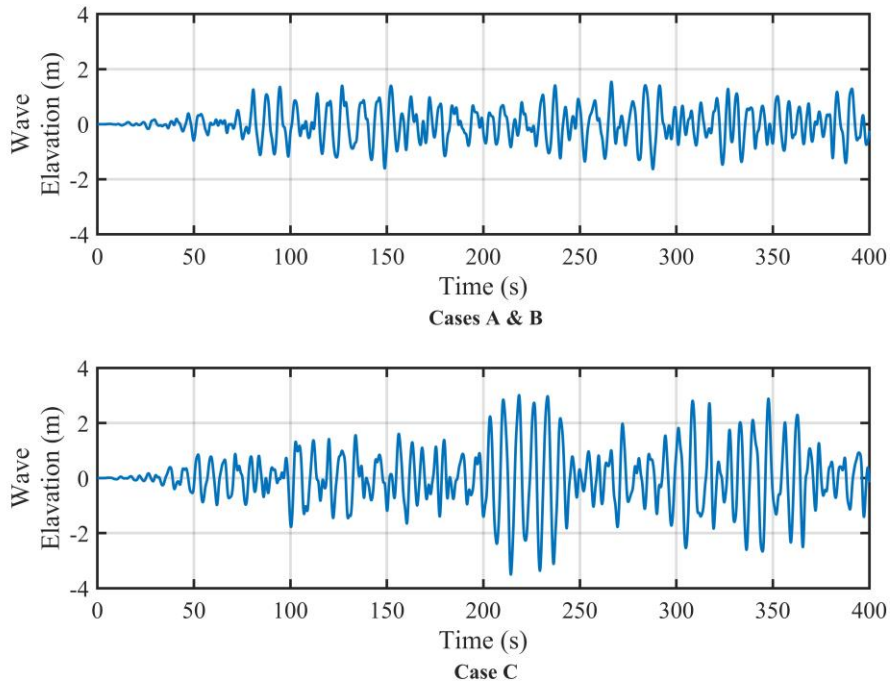


Figure 16: Wave elevation profile during the performance of the WEC for the 3 cases

First, we compare the flap's oscillation in cases A and B in Figure 17. Since these two have the same wave characteristics but different PTO configurations, one can assign almost all the difference in oscillation to the PTO stiffness and damping. Both parameters are virtually trivial in case A and come into effect in case B. It can be seen that the PTO C and K in isolation dampen the flap's oscillations, both the motion and the velocity. For case C, the flap's fluctuation during the simulation almost mimics the shape of the wave elevation, which is predictable. But the maximum flap motion roughly occurs in $t = 125$ s of case A.

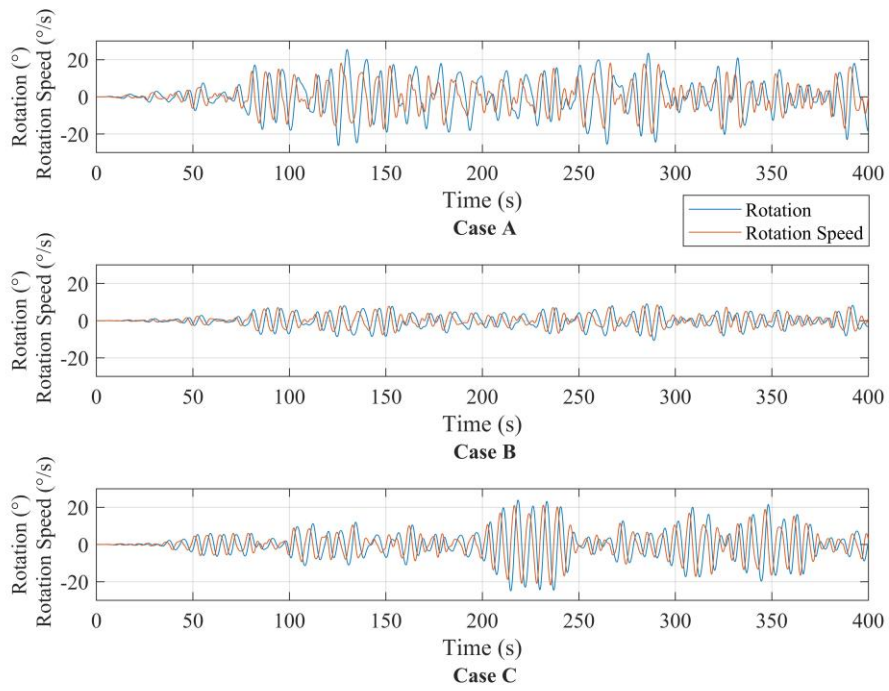


Figure 17: Flap's oscillations motion and velocity the 3 cases

Next, in Figure 18 the PTO force and power output for the 3 cases are presented. Note that for this purpose, the y-axis for the 3 cases is modified for more clear visualization. According to the y-axis, it can be said that roughly case B produces ten times more power the case A produces. And that case C generates 50 times more the case A.

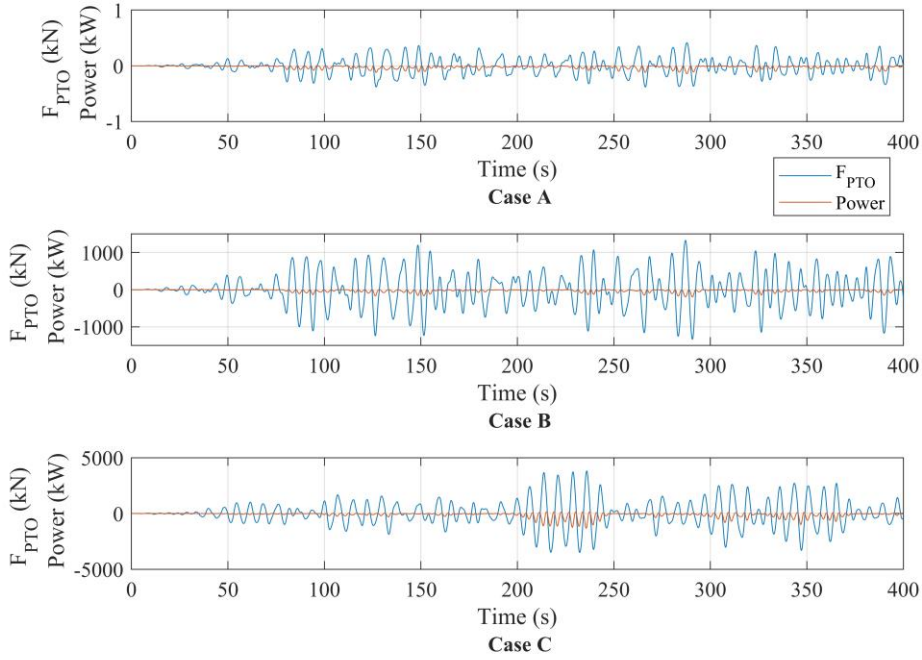
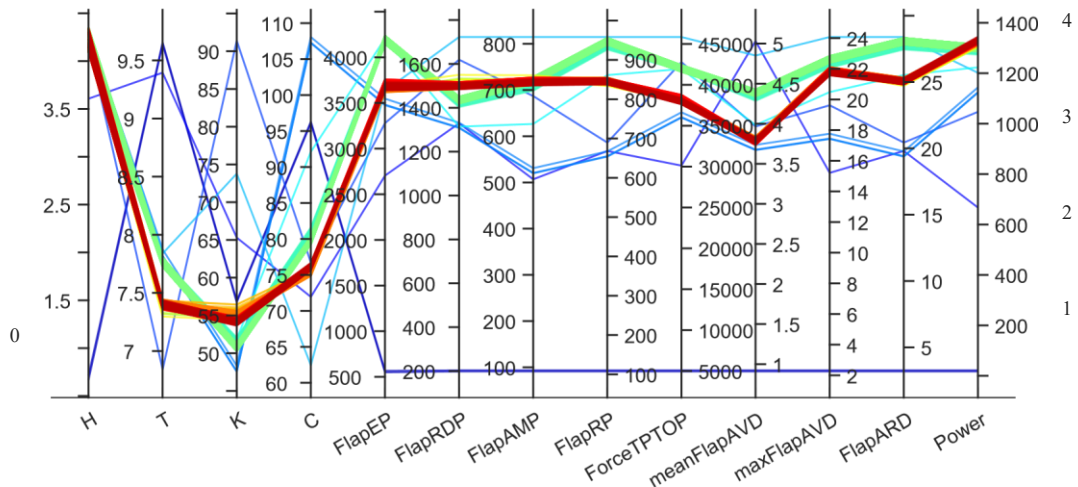


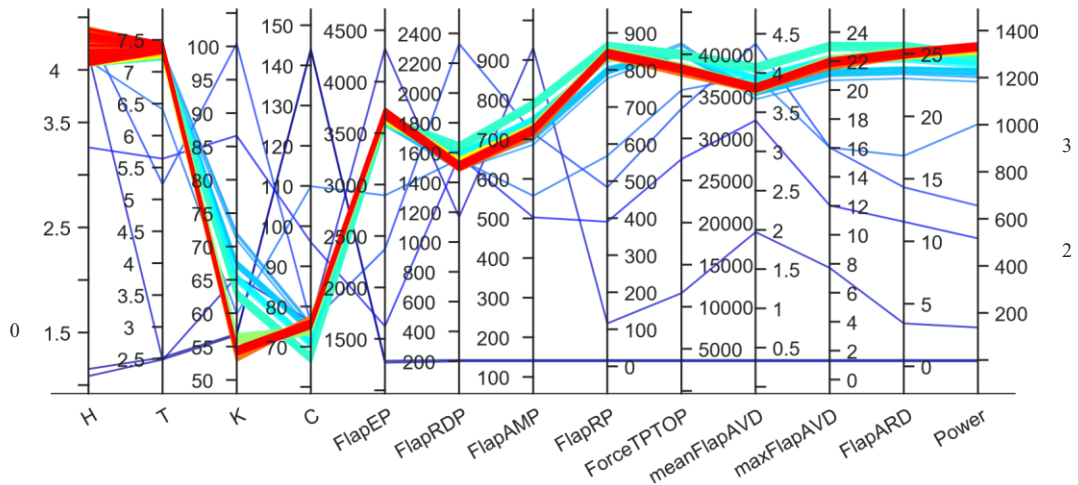
Figure 18: PTO force and power output for the 3 cases

For case C, the PTO force is peaking during the 200 s and 250 s marks due to the substantial wave magnitude (see Figure 16). This happens multiple times to a lesser extent at different times during the simulation (100-140 s, 155-165 s, 175-180 s, 270-375 s). Similarly, it can be seen for case B that the highest power outputs occur when the PTO force is at max. But overall, the extent of the produced power is about five times smaller, which can be attributed to the PTO mechanical parameters. Finally, for case A, the default WEC-Sim case, considering the PTO stiffness coefficient is zero and the damping coefficient is very low, the generated power is almost between 500 and 1000 times smaller than the best-found sample in case C. In the context of optimizing the power output of a WEC, parallel coordinate plots can be helpful in understanding the relationships between the optimization parameters (such as damping, stiffness, wave height, and period) and the resulting power output. For example, in Figure 19, we can observe that increasing the damping and stiffness of the WEC leads to a decline in power output, while increasing the wave height leads to an upsurge in power output.

Figure 19 showcases the parallel plots for the two selected runs of the HC-EGWO in order to achieve the highest power output; this includes the best-found solution by all the ten optimization runs. Furthermore, by analyzing the lines corresponding to each parameter in this Figure, it can be achievable to identify the range of parameter values that lead to optimal power output; for instance, the optimal ranges of K and C are [50-65] and [70-80], respectively. Another significant observation from the parallel plots is that there are sharp, non-linear relationships between the optimization parameters and the power output of the WEC.



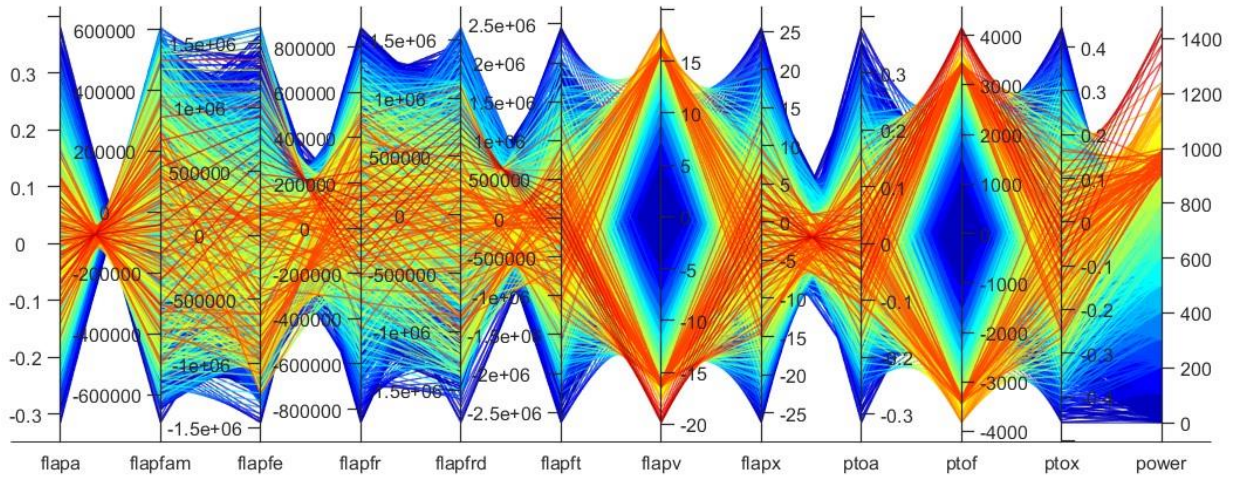
(a)



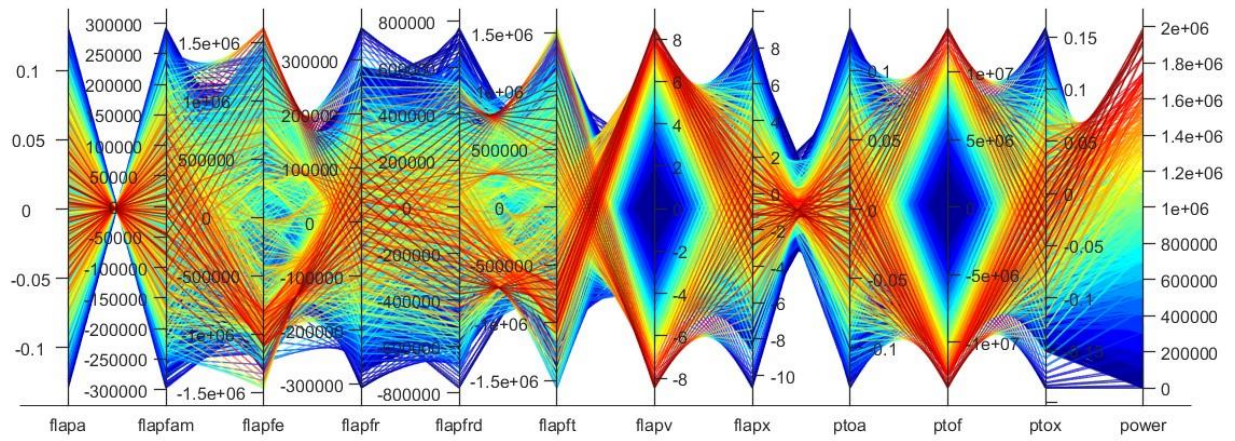
(b)

Figure 19: Two examples of the best-performed optimization method’s exploration through the decision variables (H, T, K, and C) with internal parameters of the simulator listed in Table 4, plus the average of total power output distribution visualized by a parallel coordinates plot. The dark red lines indicate the highest absorbed power output based on the configurations. (in the figures, the H, T, K, and C are the input parameters. FlapEP, FlapRD, and FlapAMP are, respectively, the excitation, radiation damping, and added mass torques, and the ForceTPTOP is the PTO force. The meanFlapAVD and maxFlapAVD are the average and maximum angular velocity of the flap, the FlapARD is the flap’s angular rotation of the flap, respectively, and the Power is the average power output of the system.)

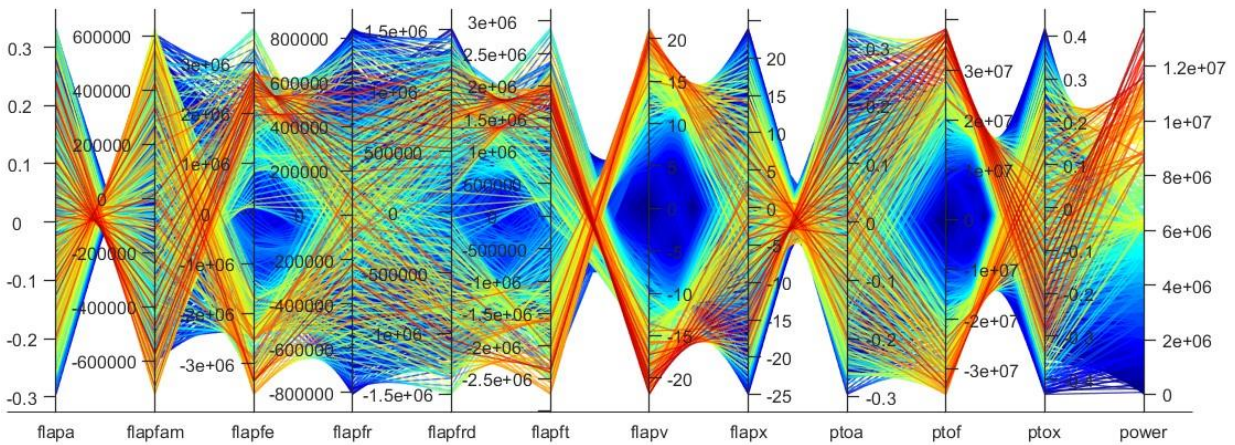
Figure 20 shows the parallel plots for the three scenarios studied in the result (See Section 6.3). These data are in real-time during the simulation time. Next, all the y-axis, except for the power output, are symmetrical, showcasing the device’s oscillating nature and, therefore, its parameters. But when taking a closer look at case A (Figure 20(a)), it is visible that the only parameters that have the simultaneous maximum as the power output (red lines) are the flap’s angular velocity and PTO force, this is consistent with equations for calculating the power output in WEC-Sim in earlier sections of the study. And also corresponds to the moderate values of the flap’s acceleration, restoring torque, excitation torque, and other hydrodynamic forces. Based on case C (Figure 20(c)), it can be seen that low absolute values of excitation force correspond to low power. Since both these parameters positively correlate with wave height, that is consistent with the theory. Notably, not every hydrodynamic force has the same trajectory as the power; for instance, the restoring force’s maximum absolute values coincide with the lowest power outputs. Since the flap’s restoring torque is dependent on the flap’s displacement only, we can see that the displacement alone can not lead to the best performance. The flap’s velocity can be considered a more critical and deciding factor.



(a)



(b)



(c)

Figure 20: Parallel interactions plot for the average of total power output distribution based on three scenarios described in the Result section. The technical details of the variables are listed in Table 4.

6.4. Sensitivity Analysis

Sensitivity analysis is a crucial mechanism in post-processing optimization methods due to identifying the most significant factors affecting the efficiency of the optimized models [68]. Table 7-Case C reports the best configuration of decision variables (H, T, K, and C) and internal hydrodynamic parameters of the simulator proposed by the HCEGWO. Meanwhile, the sensitivity analysis results can be seen in Figure 21. The black lines show the unfeasible areas of the search space for K (Figure 21(c)) and C (Figure 21(d)). The power output of the best-found solution discovered by sensitivity analysis was 1333.1 (kW). This negligible improvement can confirm that the proposed optimization method (HC-EGWO) is able to explore comprehensively the search space and converge to an appropriate solution.

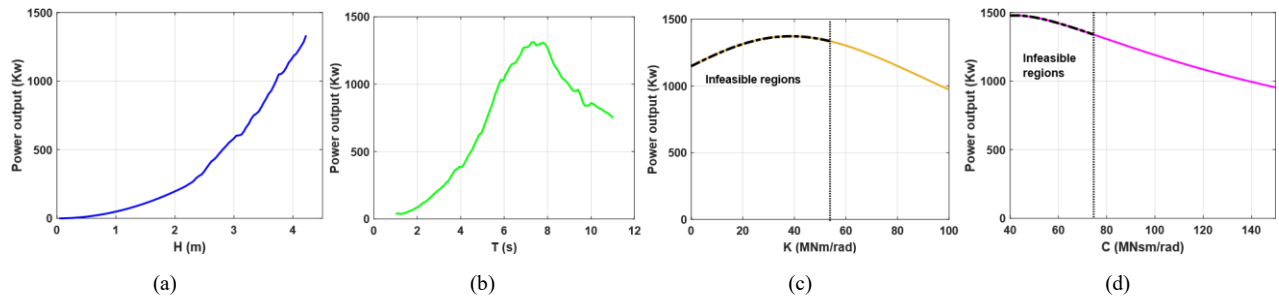


Figure 21: Sensitivity analysis of the best-found configuration using the proposed hybrid optimisation method.

6.5. Site Selection

In the last segment, an operational spot will be selected as the best location for the installation of the device. This is obtained by analyzing the best-found solution and finding the location from the 105 initial data points in the Caspian Sea that has the closest wave characteristic values, namely wave height and wave period, to the theoretic best location. The optimum values are $H = 4.223$ m and $T = 7.39$ s. Then, the best location was found using a Root Mean Square Error method (Figure 22), and the RMSE values for all the data points were evaluated. In the end, a data point belonging to the Kiashahr Port resulted in $RMSE = 2.78$, which was the minimum among the analyzed spots. The longitude and latitude of the best-found location are 37.6° N 50.1° E; this spot belongs to the Kiashahr Port.

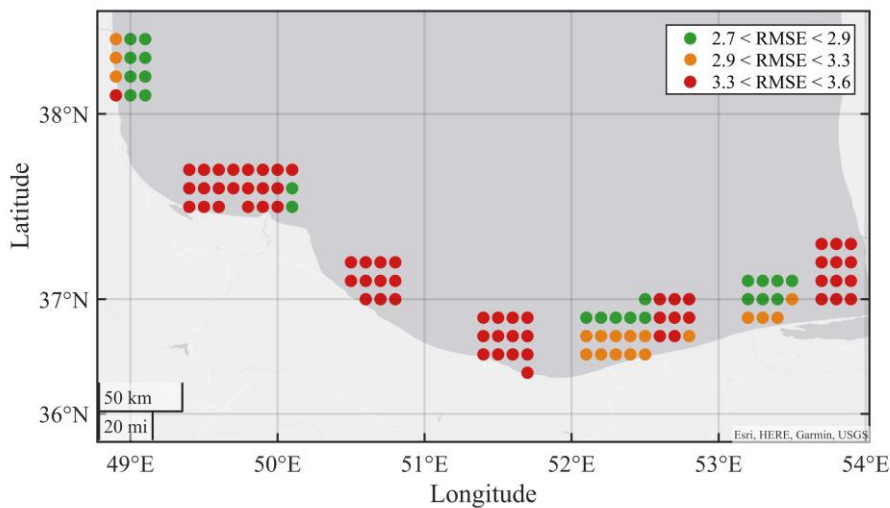


Figure 22: Categorization of the 105 data points based on the fitness of their wave significant height and peak period (using the RMSE method)

7. Conclusion

This study focused on optimizing the power take-off (PTO) parameters and site selection for an offshore oscillating surge wave energy converter (OSWEC) in the Caspian Sea. The optimization was performed using the novel Hill Climbing Explorative Gray Wolf Optimizer (HC-EGWO), which showed strong performance across 16 benchmark multimodal functions. When applied to the OSWEC case study, the HC-EGWO discovered a high-quality solution that increased the power output by approximately 3% compared to other methods.

The results provide valuable insights into the complex interplay between the converter's mechanical design and the surrounding wave climate. Specifically, the sensitivity analyses revealed that wave height and PTO damping have the most substantial impact on the power output. Increasing the wave height boosts the absorbed power, while lower PTO damping is preferable. Meanwhile, moderate values of wave period and PTO stiffness lead to the highest outputs. There are also non-linear relationships and trade-offs between the parameters influencing the hydrodynamic forces acting on the device.

Overall, the proposed HC-EGWO algorithm proved effective in handling this challenging multimodal optimization problem. The hybridization with local search prevented premature convergence and bolstered the exploration of the solution space. The outcomes showcase the method's capabilities for optimizing offshore renewable energy systems where complex hydrodynamic interactions are involved. They provide a valuable starting point for devising control strategies that ensure OSWECs operate safely within extreme seas while maximizing power generation.

Moreover, the results offer insights into deploying OSWECs in the unique conditions of the Caspian Sea. The landscape analysis of available wave data from the region informed the creation of feasible parameter bounds. And the site selection analysis pinpointed a location with strong energy potential based on the optimal wave height and period found by the HC-EGWO. Hence, the outcomes provide a launchpad for harnessing the vast untapped wave resources of the Caspian basin.

Future work can focus on incorporating more advanced hydrodynamic modeling into the WEC simulations. The effects of viscosity, turbulence, and non-linear waves could be accounted for using computational fluid dynamics. Additionally, real-world PTO systems like hydraulic and direct-drive PTOs can be simulated to optimize their parameters. Finally, expanding the optimization to more complex problems like WEC arrays and combining it with control strategy optimization represents promising research directions.

References

- [1] Mehmet Melikoglu. Current status and future of ocean energy sources: A global review. *Ocean Engineering*, 148:563–573, 2018.
- [2] Huakun Hu, Wendong Xue, Peng Jiang, and Yong Li. Bibliometric analysis for ocean renewable energy: An comprehensive review for hotspots, frontiers, and emerging trends. *Renewable and Sustainable Energy Reviews*, 167:112739, 2022.
- [3] Weixing Chen, Xionsen Lin, Yunfei Lu, Shaoxun Li, Lucai Wang, Yongkuang Zhang, and Feng Gao. Design and experiment of a doublewing wave energy converter. *Renewable Energy*, 202:1497–1506, 2023.
- [4] Erfan Amini, Hossein Mehdipour, Emilio Faraggiana, Danial Golbaz, Sevda Mozaffari, Giovanni Bracco, and Mehdi Neshat. Optimization of hydraulic power take-off system settings for point absorber wave energy converter. *Renewable Energy*, 194:938–954, 2022.
- [5] Danial Golbaz, Rojin Asadi, Erfan Amini, Hossein Mehdipour, Mahdieh Nasiri, Bahareh Etaati, Seyed Taghi Omid Naeeni, Mehdi Neshat, Seyedali Mirjalili, and Amir H Gandomi. Layout and design optimization of ocean wave energy converters: A scoping review of state-of-the-art canonical, hybrid, cooperative, and combinatorial optimization methods. *Energy Reports*, 8:15446–15479, 2022.
- [6] Benjamin Drew, Andrew R Plummer, and M Necip Sahinkaya. A review of wave energy converter technology, 2009.
- [7] A Abazari and MM Azimnia. Enhanced power extraction by splitting a single flap-type wave energy converter into a double configuration. *Renewable Energy Research and Applications*, 2022.
- [8] Yong Cheng, Lianyang Tang, and Chunyan Ji. Three-dimensional hydrodynamic analysis and efficiency optimization of submerged multicylindrical oscillating wave surge converter. *Ocean Engineering*, 215:107710, 2020.
- [9] Nima Ghasemipour, Pouria Izanlou, and Mohammad Hossein Jahangir. Feasibility study on utilizing oscillating wave surge converters (owscs) in nearshore regions, case study: Along the southeastern coast of iran in oman sea. *Journal of Cleaner Production*, 367:133090, 2022.
- [10] Matthew Folley, TJT Whittaker, and Alan Henry. The effect of water depth on the performance of a small surging wave energy converter. *Ocean Engineering*, 34(8-9):1265–1274, 2007.
- [11] Matthew Folley, Trevor Whittaker, and J Van't Hoff. The design of small seabed-mounted bottom-hinged wave energy converters. In *Proceedings of the 7th European wave and tidal energy conference*, volume 455, page 312. Citeseer, 2007.

- [12] Emiliano Renzi and Frederic Dias. Hydrodynamics of the oscillating wave surge converter in the open ocean. *European Journal of Mechanics B/Fluids*, 41:1–10, 2013.
- [13] R Porter and NRT Biggs. Wave energy absorption by a flap-type oscillating wave surge converter. *University of Bristol–Department of Mathematics–Study*. Available online: <http://www.maths.bris.ac.uk/marp/publications.html> (accessed on 6 April 2016), 2012.
- [14] Michael A Choiniere, Nathan M Tom, and Krish P Thiagarajan. Load shedding characteristics of an oscillating surge wave energy converter with variable geometry. *Ocean Engineering*, 186:105982, 2019.
- [15] Zhenqing Liu, Yize Wang, and Xugang Hua. Numerical studies and proposal of design equations on cylindrical oscillating wave surge converters under regular waves using sph. *Energy Conversion and Management*, 203:112242, 2020.
- [16] RPF Gomes, MFP Lopes, JCC Henriques, LMC Gato, and AFO Falcao. The dynamics and power extraction of bottom-hinged plate wave energy converters in regular and irregular waves. *Ocean Engineering*, 96:86–99, 2015.
- [17] Shou-qiang Qiu, Jia-wei Ye, Dong-jiao Wang, and Fu-lin Liang. Experimental study on a pendulum wave energy converter. *China Ocean Engineering*, 27(3):359–368, 2013.
- [18] Chen-Chou Lin, Yi-Chih Chow, and Shiao-Yih Tzang. The viscous effect in power capture of bottom-hinged oscillating wave surge converters. In *Proceedings of the 4rd Asian Wave and Tidal Energy Conference (AWTEC), Taipei, Taiwan*, pages 423–1.
- [19] Alexis Merigaud and John V Ringwood. A nonlinear frequency-domain approach for numerical simulation of wave energy converters. *IEEE Transactions on Sustainable Energy*, 9(1):86–94, 2017.
- [20] Yi-Hsiang Yu and Ye Li. Reynolds-averaged navier–stokes simulation of the heave performance of a two-body floating-point absorber wave energy system. *Computers & Fluids*, 73:104–114, 2013.
- [21] Pal Schmitt, Henrik Asmuth, and Björn Elsäßer. Optimising power take-off of an oscillating wave surge converter using high fidelity numerical simulations. *International journal of marine energy*, 16:196–208, 2016.
- [22] Josh Davidson and Ronan Costello. Efficient nonlinear hydrodynamic models for wave energy converter design—a scoping study. *Journal of Marine Science and Engineering*, 8(1):35, 2020.
- [23] Yi-Hsiang Yu Adam Keester Nathan Tom Dominic Forbush Jorge Leon Jeff Grasberger Salman Husain Kelley Ruehl, David Ogden. Wec-sim v5.0.1, 2022.
- [24] Jian Tan, Henk Polinder, Antonio Jarquin Laguna, and Sape Miedema. A wave-to-wire analysis of the adjustable draft point absorber wave energy converter coupled with a linear permanent-magnet generator. *Ocean Engineering*, 276:114195, 2023.
- [25] Cole Burge, Nathan Tom, Krish Thiagarajan, Jacob Davis, and Nhu Nguyen. Performance modeling of a variable-geometry oscillating surge wave energy converter on a raised foundation. In *International Conference on Offshore Mechanics and Arctic Engineering*, volume 85192, page V009T09A010. American Society of Mechanical Engineers, 2021.
- [26] Salman Husain, Jacob Davis, Nathan Tom, Krish Thiagarajan, Cole Burge, and Nhu Nguyen. Influence on structural loading of a wave energy converter by controlling variable-geometry components and the power take-off. In *International Conference on Offshore Mechanics and Arctic Engineering*, volume 85932, page V008T09A087. American Society of Mechanical Engineers, 2022.
- [27] Erfan Amini. *Locating, designing and evaluating the Oscillating Surge Wave Energy Converter using Grey Wolf Optimizer algorithm*. PhD thesis, University of Tehran, 2019.
- [28] Michael Choiniere, Jacob Davis, Nhu Nguyen, Nathan Tom, Matthew Fowler, and Krish Thiagarajan. Hydrodynamics and load shedding behavior of a variable-geometry oscillating surge wave energy converter (oswec). *Renewable Energy*, 194:875–884, 2022.
- [29] Bret Bosma, Asher Simmons, Pedro Lomonaco, Kelley Ruehl, and Budi Gunawan. wec-sim phase 1 validation testing: experimental setup and initial results. In *International Conference on Offshore Mechanics and Arctic Engineering*, volume 49972, page V006T09A025. American Society of Mechanical Engineers, 2016.
- [30] Kelley Ruehl, Carlos Michelen, Bret Bosma, and Yi-Hsiang Yu. Wec-sim phase 1 validation testing: numerical modeling of experiments. In *International Conference on Offshore Mechanics and Arctic Engineering*, volume 49972, page V006T09A026. American Society of Mechanical Engineers, 2016.
- [31] Jia Mi, Jianuo Huang, Xiaofan Li, Lisheng Yang, Alaa Ahmed, Raju Datla, Matt Folly, Muhammad Hajj, and Lei Zuo. Dual-flap floating oscillating surge wave energy converter: Modelling and experiment evaluation. *IFAC-PapersOnLine*, 55(27):138–143, 2022.
- [32] VVS Sricharan and Srinivasan Chandrasekaran. Time-domain analysis of a bean-shaped multi-body floating wave energy converter with a hydraulic power take-off using wec-sim. *Energy*, 223:119985, 2021.
- [33] Michael Lawson, Yi-Hsiang Yu, Kelley Ruehl, Carlos Michelen, et al. Development and demonstration of the wec-sim wave energy converter simulation tool. 2014.
- [34] Michael A Choiniere, Krish Thiagarajan, and Nathan M Tom. Study of a novel oscillating surge wave energy converter. *Proceedings of Offshore Energy and Storage*, (1):1–11, 2017.
- [35] Wanan Sheng and Anthony Lewis. Power takeoff optimization for maximizing energy conversion of wave-activated bodies. *IEEE Journal of Oceanic Engineering*, 41(3):529–540, 2016.
- [36] Wanan Sheng and Anthony Lewis. Power takeoff optimization to maximize wave energy conversions for oscillating water column devices. *IEEE Journal of Oceanic Engineering*, 43(1):36–47, 2017.
- [37] Christopher J Cargo, Andrew R Plummer, Andrew J Hillis, and Michael Schlotter. Determination of optimal parameters for a hydraulic power take-off unit of a wave energy converter in regular waves. *Proceedings of the Institution of Mechanical Engineers, Part A: Journal of Power and Energy*, 226(1):98–111, 2012.
- [38] Dahai Zhang, Haocai Huang, Ying Chen, Haitao Zhao, and Wei Li. State-dependent model of a hydraulic power takeoff for an inverse pendulum wave energy converter. *Marine Technology Society Journal*, 49(5):38–48, 2015.
- [39] Wei Zhang. Parameter adjustment strategy and experimental development of hydraulic system for wave energy power generation. *Symmetry*, 12(5):711, 2020.

- [40] Hong-Wei Fang, Yu-Zhu Feng, and Guo-Ping Li. Optimization of wave energy converter arrays by an improved differential evolution algorithm. *Energies*, 11(12):3522, 2018.
- [41] RPF Gomes, JCC Henriques, LMC Gato, and AF de O Falcao. Hydrodynamic optimization of an axisymmetric floating oscillating water column for wave energy conversion. *Renewable Energy*, 44:328–339, 2012.
- [42] Soheil Esmailzadeh and Mohammad-Reza Alam. Shape optimization of wave energy converters for broadband directional incident waves. *Ocean Engineering*, 174:186–200, 2019.
- [43] Jianyang Lyu, Ossama Abdelkhalik, and Lucia Gauchia. Optimization of dimensions and layout of an array of wave energy converters. *Ocean Engineering*, 192:106543, 2019.
- [44] Anna Garcia-Teruel, Bryony DuPont, and David IM Forehand. Hull geometry optimisation of wave energy converters: On the choice of the optimisation algorithm and the geometry definition. *Applied Energy*, 280:115952, 2020.
- [45] Chunyuan Liu, Yi Chen, Rui Dong, and Baolin Ye. Optimization design of tubular permanent magnet linear generator based on entropy model for wave energy conversion. Available at SSRN 4312827.
- [46] Judicael Aubry, Hamid Ben Ahmed, and Bernard Multon. Sizing optimization methodology of a surface permanent magnet machine-converter system over a torque-speed operating profile: Application to a wave energy converter. *IEEE Transactions on Industrial Electronics*, 59(5):2116–2125, 2011.
- [47] Mehdi Neshat, Nataliia Y Sergiienko, Seyedali Mirjalili, Meysam Majidi Nezhad, Giuseppe Piras, and Davide Astiaso Garcia. Multi-mode wave energy converter design optimisation using an improved moth flame optimisation algorithm. *Energies*, 14(13):3737, 2021.
- [48] Nan Zhang, Chen Feng, Yahui Shan, Na Sun, Xiaoming Xue, and Liping Shi. A universal stability quantification method for grid-connected hydropower plant considering fopci controller and complex nonlinear characteristics based on improved gwo. *Renewable Energy*, 211:874–894, 2023.
- [49] Qiyue Xie, Ziqi Guo, Daifei Liu, Zhisheng Chen, Zhongli Shen, and Xiaoli Wang. Optimization of heliostat field distribution based on improved gray wolf optimization algorithm. *Renewable Energy*, 176:447–458, 2021.
- [50] Gleb S Dyakonov and Rashit A Ibrayev. Long-term evolution of caspian sea thermohaline properties reconstructed in an eddy-resolving ocean general circulation model. *Ocean Science*, 15(3):527–541, 2019.
- [51] Mohammad Hossein Jahangir and Mehran Mazinani. Evaluation of the convertible offshore wave energy capacity of the southern strip of the caspian sea. *Renewable Energy*, 152:331–346, 2020.
- [52] Sadaf Nasrollahi, Aliyeh Kazemi, Mohammad-Hossein Jahangir, and Sara Aryaee. Selecting suitable wave energy technology for sustainable development, an mcdm approach. *Renewable Energy*, 202:756–772, 2023.
- [53] S Taebi and A Golshani. Long term characteristics of waves in the caspian sea, the persian gulf and the gulf of oman. *COPEDEC VII*, 2008.
- [54] Joseph Van't Hoff. *Hydrodynamic modelling of the oscillating wave surge converter*. PhD thesis, Queen's University Belfast, 2009.
- [55] R Gomes, M Lopes, JCC Henriques, LMC Gato, and AFO Falcao. A study on the wave energy conversion by submerged bottom-hinged plates. In *9th European Wave and Tidal Energy Conference, Southampton, UK*, 2011.
- [56] Koray Senol and Mehdi Raessi. Enhancing power extraction in bottom-hinged flap-type wave energy converters through advanced power take-off techniques. *Ocean Engineering*, 182:248–258, 2019.
- [57] Michael Kelly, Nathan Tom, Yi-Hsiang Yu, Alan Wright, and Michael Lawson. Annual performance of the second-generation variable geometry oscillating surge wave energy converter. *Renewable Energy*, 177:242–258, 2021.
- [58] Seyedali Mirjalili, Seyed Mohammad Mirjalili, and Andrew Lewis. Grey wolf optimizer. *Advances in engineering software*, 69:46–61, 2014.
- [59] Nitin Mittal, Urvinder Singh, and Balwinder Singh Sohi. Modified grey wolf optimizer for global engineering optimization. *Applied Computational Intelligence and Soft Computing*, 2016, 2016.
- [60] Wen Long, Jianjun Jiao, Ximing Liang, and Mingzhu Tang. An exploration-enhanced grey wolf optimizer to solve high-dimensional numerical optimization. *Engineering Applications of Artificial Intelligence*, 68:63–80, 2018.
- [61] Muhammad Hamza Zafar, Noman Mujeeb Khan, Adeel Feroz Mirza, and Majad Mansoor. Bio-inspired optimization algorithms based maximum power point tracking technique for photovoltaic systems under partial shading and complex partial shading conditions. *Journal of Cleaner Production*, 309:127279, 2021.
- [62] Xiang Ma, Duan Jiandong, Wang Xiao, Song Tuo, Wang Yanhang, and Song Ting. Research of photovoltaic systems mppt based on improved grey wolf algorithm under partial shading conditions. In *2018 2nd IEEE Conference on Energy Internet and Energy System Integration (EI2)*, pages 1–6. IEEE, 2018.
- [63] Wen Long, Shaohong Cai, Jianjun Jiao, and Mingzhu Tang. An efficient and robust grey wolf optimizer algorithm for large-scale numerical optimization. *Soft Computing*, 24(2):997–1026, 2020.
- [64] Anbo Meng, Cong Zeng, Peng Wang, De Chen, Tianmin Zhou, Xiaoying Zheng, and Hao Yin. A high-performance crisscross search based grey wolf optimizer for solving optimal power flow problem. *Energy*, 225:120211, 2021.
- [65] Nicolas Quartier. Numerical implementation of the power-take-off (pto) of two types of generic wave energy converters using wec-sim. *Ghent University*, 2018.
- [66] Katie M Brodersen, Emily A Bywater, Alec M Lanter, Hayden H Schennum, Kumansh N Furia, Maulee K Sheth, Nathaniel S Kiefer, Brittany K Cafferty, Akshay K Rao, Jose M Garcia, et al. Direct-drive ocean wave-powered batch reverse osmosis. *Desalination*, 523:115393, 2022.
- [67] Honggui Han, Xiaolong Wu, Hongxu Liu, and Junfei Qiao. An efficient optimization method for improving generalization performance of fuzzy neural networks. *IEEE Transactions on Fuzzy Systems*, 27(7):1347–1361, 2018.
- [68] Andrea Saltelli, Ksenia Aleksankina, William Becker, Pamela Fennell, Federico Ferretti, Niels Holst, Sushan Li, and Qiongli Wu. Why so many published sensitivity analyses are false: A systematic review of sensitivity analysis practices. *Environmental Modelling & Software*, 114:29–39, 2019.